Ultramafic lavas and high-Mg basaltic dykes from the Othris ophiolite complex, Greece☆

Ioannis Baziotis [a,*], Maria Economou-Eliopoulos [b], Paul D. Asimow [c]

[a] Department of Natural Resources Management and Agricultural Engineering, Agricultural University of Athens, Iera Odos 75, 11855 Athens, Greece
[b] Department, of Geology & Geoenvironment, Section of Economic Geology & Geochemistry, National University of Athens, Panepistimiopolis, 15784 Athens, Greece
[c] California Institute of Technology, Division of Geological and Planetary Sciences, Pasadena, CA 91125, USA

A B S T R A C T

We evaluate the petrography and geochemistry of an unusual suite of subduction-related Phanerozoic high-MgO rocks from the Othris ophiolite complex in Greece, some of which have previously been described as komatiitic lavas. In particular, we study ultramafic, olivine-phyric lavas from the Agrilia area and high-Mg basaltic dykes from the Pournari area. We seek to define primary magmatic MgO contents and initial liquidus temperatures as well as the differentiation sequence and cooling rates experienced by the lavas and dykes. One of our goals is to relate the Othris case to known komatiite and boninite occurrences and to address whether Othris documents an important new constraint on the temporal evolution of ambient mantle temperature, plume-related magmatism, and subduction of oceanic lithosphere. We conclude that, despite whole-rock MgO contents of 31–33 wt%, the olivine-phyric lavas at Agrilia had an upper limit liquid MgO content of 17 wt% and are therefore picrites, not komatiites. The Agrilia lavas contain the unusual Ti-rich pyroxenoid rhönite; we discuss the significance of this occurrence. In the case of the Pournari high-Mg dykes, the distinctive dendritic or plumose clinopyroxene texture, though it resembles in some ways the classic spinifex texture of komatiites, is simply evidence of rapid cooling at the dyke margin and not evidence of extraordinarily high liquidus temperatures. We correlate the dendritic texture with disequilibrium mineral chemistry in clinopyroxene to constrain the cooling rate of the dyke margins.

© 2017 Elsevier B.V. All rights reserved.

1. Introduction

Mafic volcanism is a surface expression of the thermal state of the Earth's interior and the MgO content of magmatic liquids, in particular, is strongly sensitive to temperature. Petrologists often focus attention on particularly high-MgO lavas and dyke margins in an effort to trace the temporal and spatial distribution of mantle temperature and it has been noted that ancient lavas typically had higher MgO contents than do recent examples (Herzberg et al., 2010; Mole et al., 2014). However, the relationship between whole-rock MgO and magmatic temperature is complicated by two important factors. First, with the exception of glassy samples, rocks may be mixtures of magmatic liquids and a crystal cargo that obscures the relation between whole-rock MgO and liquid composition (Herzberg and O'Hara, 2002). Second, magmatic water shifts the temperature of olivine-liquid equilibria downwards and a hydrous magma can, in some ways, masquerade as a hot magma

(Grove and Parman, 2004; Grove et al., 2006; Kushiro, 1969). Hydrous melting has commonly been invoked to explain anomalously high-MgO lavas in Phanerozoic oceanic settings. Abbou-Kebir et al. (2015), for example, studied the northern Oman ophiolite and described hydrous melting conditions in a supra-subduction zone (SSZ) setting, leading to high degrees of melting and eruption of high-MgO lavas (21–25 wt% MgO). Similarly, high-MgO boninites have been reported from Izu-Ogasawara-Mariana arc, with inferred MgO contents between 17 and 22 wt% in the primary liquid, liquidus temperatures of 1345–1421 °C, and significantly elevated H_2O contents.

In Greece, Triassic magmatism occurred as the result of rifting and formation of an oceanic basin between the Apulia and Pelagonian microplates (e.g., Robertson and Mountrakis, 2006). Alkaline basalts erupted during the initial stages of this event due to low-degree partial melting of an enriched mantle source, evolving to ultramafic lavas as nearby subduction initiation brought about a fore-arc setting. These ultramafic lavas, outcropping today in the Othris Mountains in central Greece, are therefore a prime instance of the rare phenomenon of Phanerozoic SSZ ultramafic magmatism (Arndt and Nisbet, 1982; Dilek and Furnes, 2014; MacLeod et al., 2013; Parlak et al., 2002; Xiong et al., 2017). Within the Othris ophiolite complex, ultramafic lavas are often spatially associated with high-Mg basaltic dykes
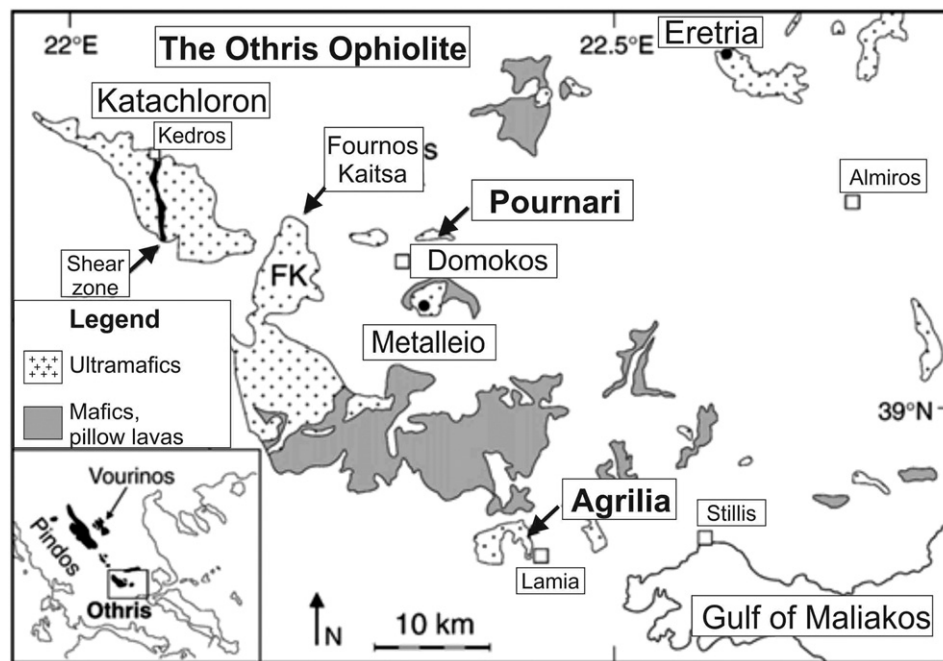

Fig. 1. Simplified geological map of the Othris Ophiolite showing the location of the study area (after Rassios and Konstantopoulou, 1993).

(Fig. 1; Barth and Gluhak, 2009; Barth et al., 2008; Cameron and Nisbet, 1982; Cameron et al., 1979; Capedri et al., 1997; Pe-Piper, 1998; Koutsovitis and Magganas, 2016; Koutsovitis et al., 2012, Saccani et al., 2011; Smith et al., 1975). In this work, we focus on the Triassic lavas of the Agrilia formation that have been previously described as komatiitic lavas (Paraskevopoulos and Economou, 1986) and on high-Mg basaltic dykes from the nearby Pournari area, respectively (Fig. 1; Economou-Eliopoulos and Paraskevopoulos, 1989; Paraskevopoulos, 1987; Paraskevopoulos and Economou, 1986; Paraskevopoulos and Economou-Eliopoulos, 1997; Tsikouras et al., 2008).

The assignment of these rocks as komatiitic lavas was based on whole-rock chemistry, but this is no longer considered a sufficient criterion for such an assignment. Despite some disagreement over the definition of komatiite, the term should be reserved for ultramafic lavas with greater than 18 wt% MgO displaying a spinifex texture (e.g., Arndt and Nisbet, 1982). We prefer the term picrite for non-spinifex olivine-phyric lavas, whose elevated whole-rock MgO content may be due to accumulated olivine, and which are mostly of Phanerozoic age (Dostal, 2008). However, applying the distinction between picrite and komatiite may require a study of the phenocryst-matrix association and an inference of liquid composition. Also, spinifex texture, either of olivine or pyroxene (Campbell and Arndt, 1982), occurs in rocks with MgO contents as low as 8 wt% MgO (Arndt, 1986). This suggests that liquid composition is not the sole determinant of whether a rock will have komatiite-like texture; instead, the physical conditions, rates, and degree of undercooling during crystallization must also be important (Arndt, 1994; Donaldson, 1976; Faure et al., 2006; Shea and Hammer, 2013; Shea et al., 2015).

In this study, we characterize the texture, modal mineralogy and chemistry of whole rocks and their constituent minerals from representative samples of the Agrilia lavas and Pournari dykes using optical microscopy, scanning electron microscopy (SEM), electron probe microanalysis (EPMA), inductively coupled plasma mass spectrometry (ICP-MS) and instrumental neutron activation analysis (INAA). We apply thermodynamic models to test whether the crystallizing phases were saturated in the liquid composition as it evolved under well-defined conditions of pressure, temperature, oxygen fugacity and water content. This approach offers more insight than simple mass balance modeling into conditions of differentiation. Since the texture formed during cooling of a lava or dyke can be controlled by gradients in time (cooling rate) or in space (local thermal gradient), we apply available experimental data and theories to distinguish the influence of flow tops and dyke walls and to show that the various constraints are internally consistent.

2. Geological setting

Major ophiolite complexes in Greece, including the Othris, Pindos and Vourinos suites (Fig. 1), were all obducted from the Middle to Late Jurassic and have been interpreted as parts of the same oceanic slab (Rassios and Moores, 2006). Differences in their geological and petrological character have been attributed to intra-slab heterogeneity. Both Mid-Ocean Ridge (MOR) and SSZ-type ophiolites (fore-arc and back-arc ridges) were obducted, tectonically fragmented and separated by overlapping sediments (Barth et al., 2008; Rassios and Moores, 2006). More specifically, the petrological and geochemical features of the Othris complex, notably the presence of large (3 Mt) chromite and compound platinum-group element (PGE) mineral deposits, have been interpreted to reflect the influence of subducted crust during a second-stage melting event (Economou-Eliopoulos and Paraskevopoulos, 1989; Economou-Eliopoulos et al., 1997; Garuti et al., 1999; Hynes, 1972). The silicate inclusions (olivine, orthopyroxene + amphibole, clinopyroxene + phlogopite, chlorite) in chromite ores resemble those in other ophiolite occurrences (e.g., Melcher et al., 1997), where they have been attributed to alkali-rich fluids during crystallization of chromite (Garuti et al., 1999). The chromite deposits in the Eretria and Domokos outcrops of the Othris complex are high in Al, Ti and V and are consistent with lower degrees of partial melting compared to the corresponding mantle section of the Vourinos complex (Economou-Eliopoulos, 1996; Hynes, 1972). In addition, the rare-earth element (REE), Ti and Zr contents; flat REE patterns; and relatively low values of Ce/Yb in opx from the Eretria harzburgite (Bizimis et al., 2000) all confirm a moderately depleted mantle for the Othris complex.

Detailed descriptions of all the mantle rock types exposed in the Othris massif have been presented by previous authors (Barth et al., 2008; Bizimis et al., 2000; Dijkstra et al., 2001) and are outside the scope of the present work, which focuses on the crustal section. The Agrilia formation is ~6 km NW of Lamia, whereas the Pournari area is

~31 km NW of Lamia. The exposed outcrops in each area cover ~2 km[2]. Both areas are mainly composed of picrites, dolerites, boninites, shales and tuffs (Economou-Eliopoulos and Paraskevopoulos, 1989). The pillow lavas are covered by ultramafic lava flows and intruded by wehrlites (Koutsovitis et al., 2012; Tsikouras et al., 2008). The picritic rocks of Agrilia, which have been previously interpreted as komatiitic lavas despite the absence of macro-spinifex texture and poor constraints on initial liquid MgO content, occur as 1–2 m thick flows composed of olivine, lesser clinopyroxene, and devitrified glassy groundmass. The studied outcrop in the Pournari area occurs in the form of late dykes (0.5–1.0 m in width) cutting the typical pillow lavas (Hynes, 1972; Paraskevopoulos and Economou-Eliopoulos, 1997).

3. Materials and methods

3.1. Petrography and mineral analysis

Polished thin sections were prepared from samples of ultramafic lavas from the Agrilia area and high-Mg basaltic dykes from the Pournari area. Thin sections were examined by transmitted and reflected light microscopy, SEM and EPMA. Melt inclusions were observed in transmitted light only in olivine and in reflected light microscopy on polished sections in chromite. Semi-quantitative analyses were carried out at the University of Athens, Department of Geology and Geoenvironment, using a JEOL JSM 5600 SEM, equipped with an automated OXFORD ISIS 300 energy dispersive X-ray analysis system. Analytical conditions were 20 kV accelerating voltage, 0.5 nA beam current, 1–2 μm beam diameter and 50 s count times. Quantitative analyses were determined in polished thin sections using a JEOL JXA 8900 Superprobe with four wavelength-dispersive spectrometers (WDS) at the Laboratory of Mineralogy and Geology, Agricultural University of Athens, Greece. All EPMA analyses used 15 kV accelerating potential. Minerals were analyzed with a 20 nA beam current, ~2 μm beam diameter, 20 s counting time on peak position and 10 s on each background position. To minimize volatile and alkali loss, glass analyses used a slightly defocused 5 μm diameter beam, 10 s on-peak and 5 s background counting times. Natural minerals were used as standards: quartz (Si), corundum (Al), albite (Na), diopside (Ca), olivine (Mg), fayalite (Fe), spessartine (Mn), orthoclase (K), apatite (P), ilmenite (Ti), chromite (Cr) and Ni-oxide (Ni), with ZAF matrix correction.

3.2. Whole-rock analysis

Major and trace element contents in whole rocks were determined by ICP-MS analysis at ACME Laboratories, Ltd, Canada. The detection limits, in weight units, stated by ACME laboratories are: 0.01% for Si—Al—Fe—Mg—Ca—K; 0.001% for Ti—Na—P; 1 part per million (ppm) for Mn—Cr—Ba—Zn—Sr—Sc; 0.1 ppm for Ni—Cu—La—Ce—Nb—Hf—Th—Zr—Y—Rb—Li; 0.2 ppm for Co (0.2 ppm); and 4.0 ppm for V. For the analyzed elements, the analytical precision is generally between 5% and 10% (from duplicate runs of standards and several unknowns), except those trace elements near the detection limit. The major element data and selected trace elements (Ni, Cr) are given in Table 1. The rest of the trace element results from ICP-MS analysis are given in Supplementary Table S1. Pt-group element (PGE) analyses were also carried out by Ni-sulfide fire-assay pre-concentration technique, as described in the appendix along with interpretation of the trace element results. These results are also in Table S1.

4. Petrography

4.1. Ultramafic lavas (Agrilia)

The ultramafic lavas from the Agrilia formation are dominated by randomly oriented phenocrysts of olivine (over 50 vol%), chromite

Table 1
Major (in wt%) elements (given in volatile-free basis) and selected trace (in ppm) elements determined by ICP-MS for ultramafic lavas and high-Mg basalts from Agrilia and Pournari areas, respectively.

Sample	Agrilia ultramafic lavas				Pournari high-Mg basaltic dykes		
	A34a	A34b	A35	A36	LM16.1	LM16.2	P.23
SiO_2	47.8	47.6	47.8	46.9	53.5	54.3	54.6
TiO_2	0.35	0.38	0.38	0.4	0.21	0.25	0.26
Al_2O_3	6.1	6.6	6.1	6.1	12.5	12	10.7
FeO_{total}	8.2	9.3	9.8	9.2	9.54	8.9	11.9
MnO	0.13	0.14	0.14	0.13	0.13	0.14	0.08
MgO	31.4	31.1	31.4	32.7	11.5	13.7	12.4
CaO	4.5	4.6	4.3	4.3	10.2	8.8	8.5
Na_2O	0.34	0.21	0.02	0.04	0.9	0.56	1.4
K_2O	0.1	0.1	0.15	0.04	0.3	0.44	0.1
P_2O_5	0.08	0.07	0.06	0.07	0.13	0.08	0.12
Total	99.0	100.1	100.2	99.9	98.9	99.1	100.1
L.O.I.	8.2	8.1	9.6	11.1	5.92	5.9	4.5
Cr	1070	1300	1400	1900	1060	900	770
Ni	1450	1400	1520	1560	290	280	210

and clinopyroxene in a devitrified glass matrix (Fig. 2A); orthopyroxene is absent. No fresh glass was found. Olivine is highly fragmented and serpentinized along cracks and margins (Fig. 2A), but is generally equant in form with no spinifex texture evident either in hand-sample or in thin-section. Olivine contains numerous, widely scattered melt inclusions, varying in size (5–20 μm) and shape (rounded and elongated). They occur as isolated glassy inclusions with spherical shrinkage bubbles (Fig. 2B–E) and as microcrystalline aggregates (Fig. 2D–F).

Fresh chromite is found disseminated within groundmass (devitrified glass) (Fig. 3A, B, E, F) and as inclusions in olivine (Fig. 3D, E, H) and clinopyroxene (Fig. 3B, G). Clinopyroxene varies in size from large, often normally zoned, phenocrysts (Fig. 3c) to fine needles. All the clinopyroxene forms are strictly surrounded by groundmass; they are never intergrown with or included in coarse olivine (Fig. 3B, D, G, H). Amphibole, rhönite, chromite, and Ti-magnetite are associated with groundmass, while serpentine and chlorite are common secondary minerals after olivine (Figs. 3, 4). Vesicles (amygdales) are dominated by chlorite. Groundmass Ti-magnetite is commonly associated with the rhönite (Fig. 4), a rare Ti-bearing pyroxenoid mineral in the aenigmatite group; we discuss the significance of its occurrence in the Agrilia groundmass below.

4.2. High-Mg basaltic dyke (Pournari)

The high-Mg basaltic dykes from Pournari are dominated by clinopyroxene (40–50 vol%), with a small proportion of orthopyroxene phenocrysts (<5 vol%) that appear to predate clinopyroxene growth (Fig. 5A) and euhedral to subhedral accessory chromite (Fig. 6). Samples taken near the wall of dyke LM16 contain needle-like acicular clinopyroxene, showing a very impressive curved branching comb and giving the illusion in some sections of a series of disconnected parts of consistent crystallographic orientation (Fig. 5). These dendrites have an ordered morphology characterized by a regular arrangement of branches along specific crystallographic axes (Figs. 5B, 6E). Dendritic clinopyroxene was not found in any samples from dyke P23 despite similar chemistry to dyke LM16 (Table 1).

5. Analytical results

5.1. Mineral chemistry

5.1.1. Silicates (olivine, clinopyroxene)

All the olivines from the Agrilia ultramafic lavas display high forsterite (Fo) contents, from $Fo_{89.9}$ to $Fo_{93.9}$. The Al_2O_3 content varies
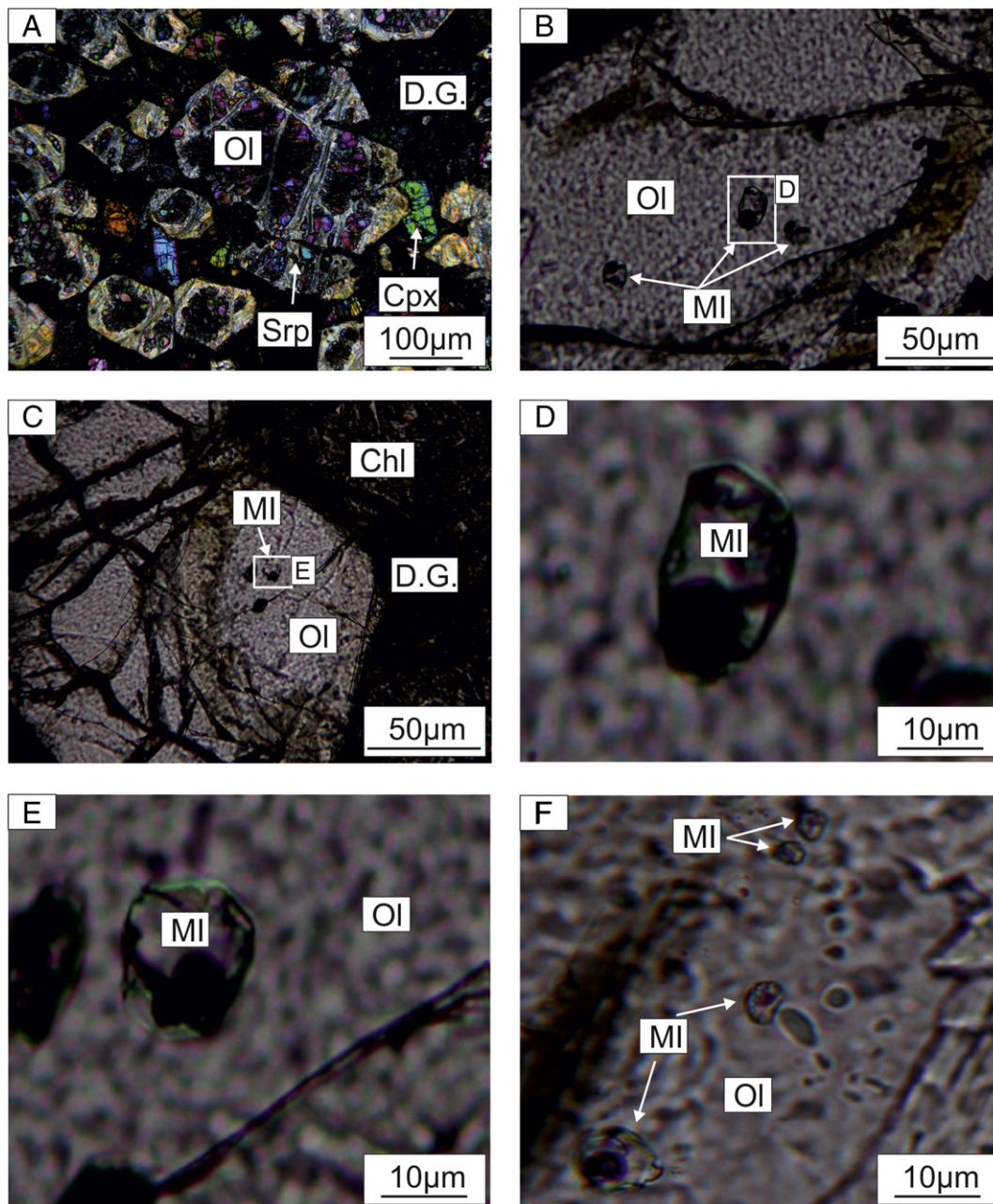
Fig. 2. Photomicrographs of ultramafic lavas from the Agrilia Formation, showing olivine (Ol), clinopyroxene (Cpx) and serpentine (Srp), in a devitrified glassy (D.G.) matrix (A) and melt inclusions (MI) in olivine crystals, occurring as isolated glassy inclusions with spherical shrinkage bubbles (B, D), microcrystalline aggregates in a chlorite (Chl)-rich matrix (C, E), or fine, two-phase inclusions with a bubble (F). A: microphotograph under crossed nicols; B–F: microphotographs under parallel nicols.

from 0.04 to 0.23 wt%, MnO from 0.05 to 0.38 wt%, and NiO from 0.28 to 0.48 wt%. The maximum Al_2O_3 value observed in the core of a $Fo_{91.6}$ olivine. The maximum MnO is found at the rim of a $Fo_{89.9}$ olivine. NiO is directly correlated with Fo content: the maximum and minimum NiO values occur in the $Fo_{93.9}$ core of an olivine and at the $Fo_{90.1}$ rim of another olivine, respectively (Fig. 7). Olivine is absent in the Pournari dykes. All the clinopyroxene in all the samples studied is augite; pigeonite is entirely absent, in contrast to the metastable dendritic pigeonite described in some rapidly quenched komatiites (Arndt and Fleet, 1979). The clinopyroxene from Agrilia is obviously zoned, showing decreasing MgO content and very well-correlated increasing Al_2O_3 and FeO^* contents (Fig. 8 and Table 2). A similar compositional variation as a function of grain size is evident among cpx crystals in the high-Mg dykes from Pournari, from large crystals to smaller spinifex-textured crystals (Table 2). The relatively large dendritic or spinifex-textured

Pounari clinopyroxene shows remarkably high and fairly uniform values of the $Mg/(Mg + Fe^T)$ ratio (0.87).

5.1.2. Oxides (chromite, Ti- magnetite)

The chromite spinel is commonly rimmed by Ti-magnetite with sharp contacts (Figs. 3H, 4C, 9). Chromite is Cr-rich, exhibiting a limited range of variation of $Cr^{3+}/(Cr^{3+} + Al^{3+})$(Cr#) 0.82–0.88 in both the Agrilia ultramafic lavas and the Pournari dykes. Lower Cr# is found only in small inclusions within cpx in one Pournari sample (Table 3; Fig. 10). TiO_2 contents of chromite range up to 0.52 wt% in the Agrilia samples but it is at or below the detection limit (0.2 wt%) in the Pournari dykes. Ti-magnetite rims at Agrilia have TiO_2 contents between 4.2 and 5.8 wt% (Table 3; Fig. 9). Ti-magnetite has much lower $Mg/(Mg + Fe^{2+})$ (Mg#), lower Cr#, and much higher $Fe^{3+}/(Cr^{3+} + Al^{3+} + Fe^{3+})$ than the chromite (Fig. 9).
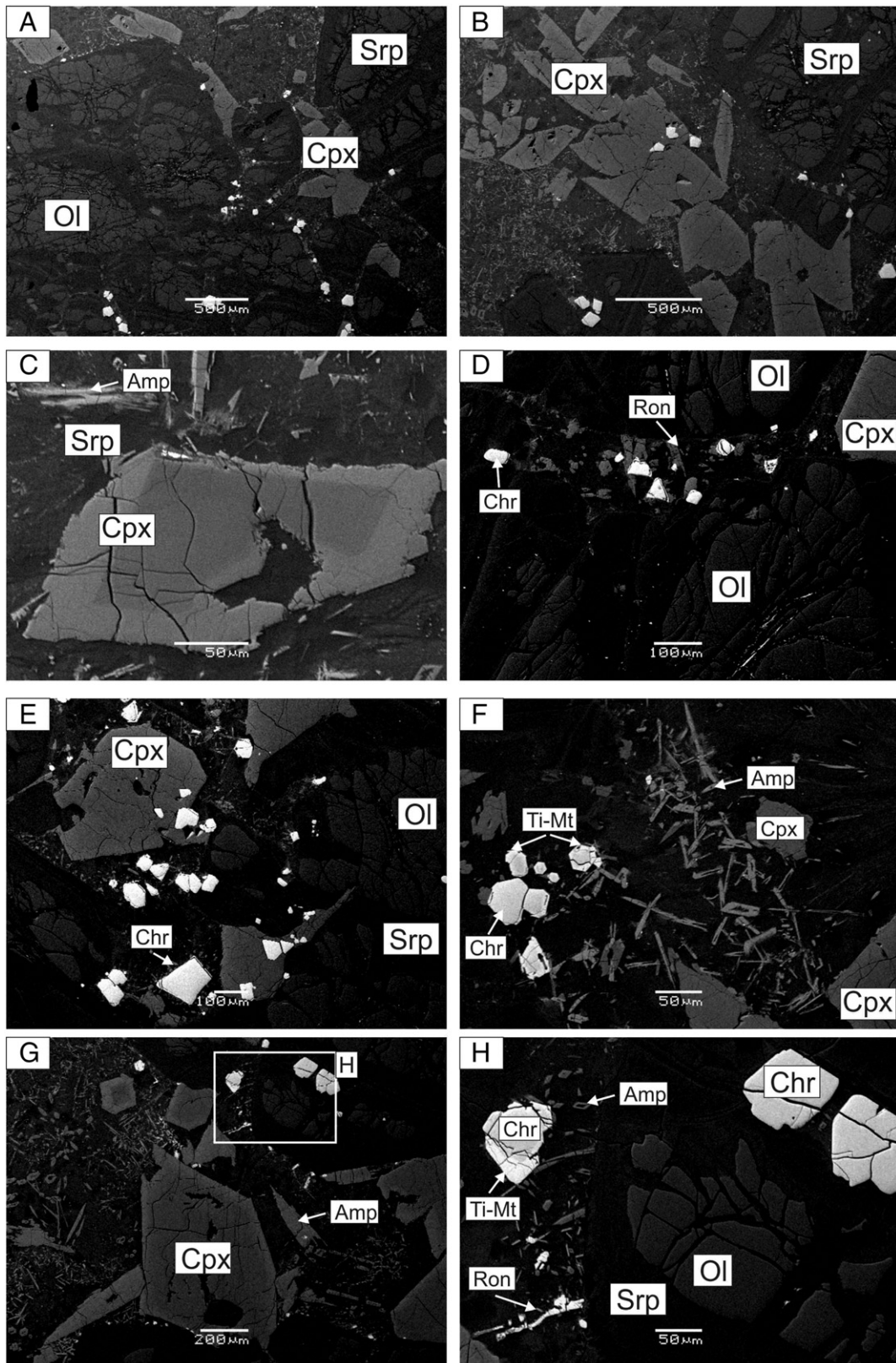
Fig. 3. Back-scattered electron (BSE) images from ultramafic lavas of the Agrilia Formation, showing the association of chromite (Chr) with olivine (A, D, E), clinopyroxene (B, E) and groundmass (A, B, D, E, F) and normally zoned clinopyroxene surrounded by amphibole (Amp) (C). Rhönite (Ron) occurs as micro-crystals (G) associated with Ti-magnetite (Ti-Mt) and randomly oriented amphibole (Amp). (H) Enlarged part of (G) showing the rhönite (>50 μm in length) and amphibole with a vertical preferred orientation in relation to the adjacent serpentinized olivine.
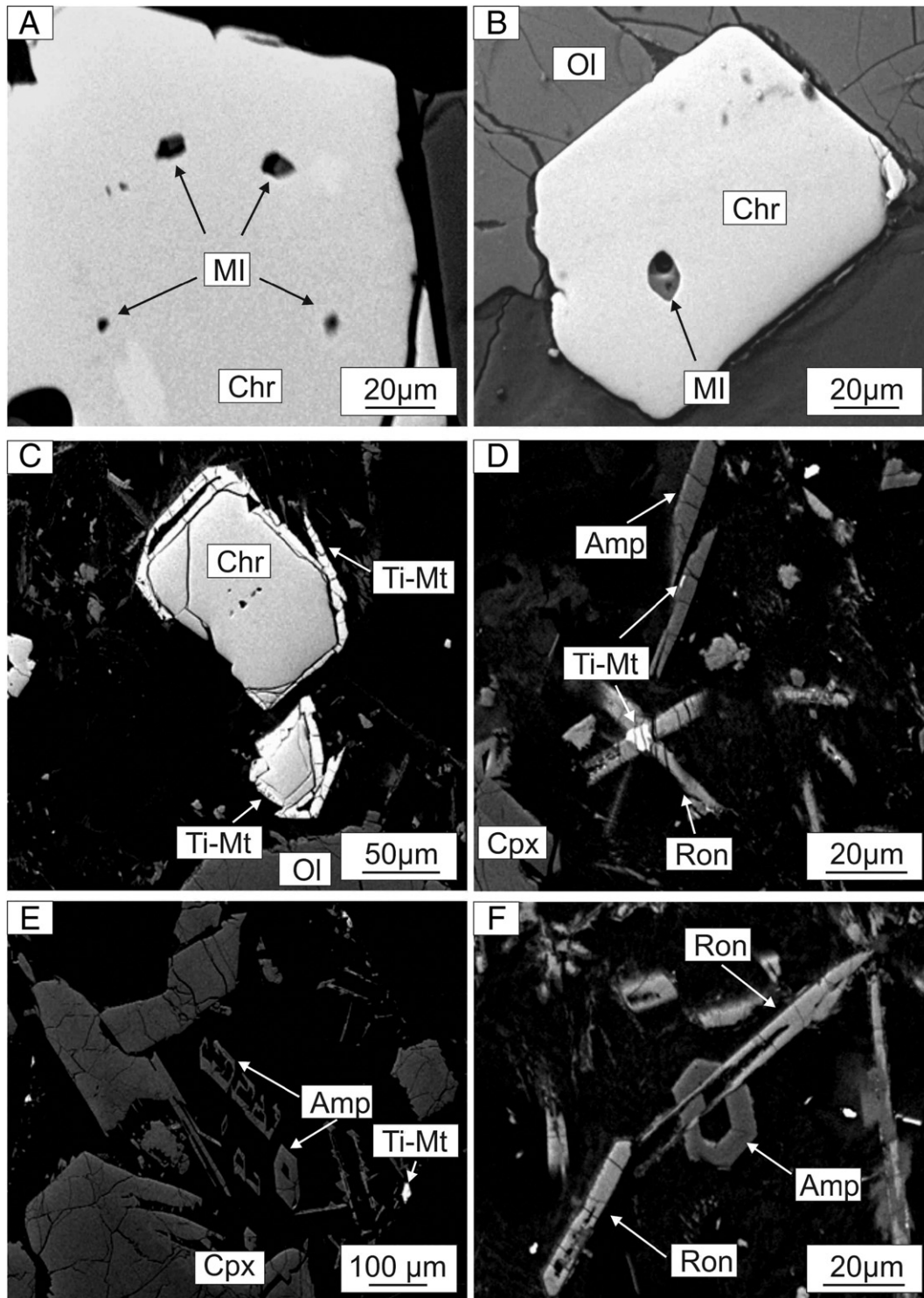
Fig. 4. Back-scattered electron (BSE) images from ultramafic lavas of the Agrilia Formation, showing melt inclusions hosted in chromite (A, B, C, black arrows), the association of Ti-bearing magnetite (Ti-Mt) with chromite (C) and rhönite (Ron)(D), Ti-bearing magnetite in the matrix (E) and rhönite with amphibole (F).

5.1.3. Rhönite

The rhönite included in devitrified glass at Agrilia has $^{VIII}Na + ^{IV}Si$ in the range 3.87–4.21 per 20 oxygen formula unit (Table 4). Plotted against $^{VIII}Ca + ^{IV}Al$, the analyses lie just below the "ideal" rhönite composition at $^{VIII}Na + ^{IV}Si = ^{VIII}Ca + ^{IV}Al = 4$ (Fig. 11). Grapes et al. (2003) argue that compositions that plot below the $\Sigma = ^{VIII}Na + ^{IV}Si + ^{VIII}Ca + ^{IV}Al = 8.0$ line reflect variable Fe^{3+} incorporation or substitution of $^{VIII}Fe^{2+}$ for Ca, and are more characteristic of rhönite formed by breakdown of

kaersutitic amphibole, as opposed to magmatic microphenocrysts of rhönite identified in basanites.

5.1.4. Melt inclusions

Although a detailed study of the melt inclusions is still in progress, preliminary results by SEM/EDS indicate that the chromite-hosted inclusions are microcrystalline aggregates of several daughter phases, including rhönite, clinopyroxene, amphibole, apatite, serpentine, and chlorite.
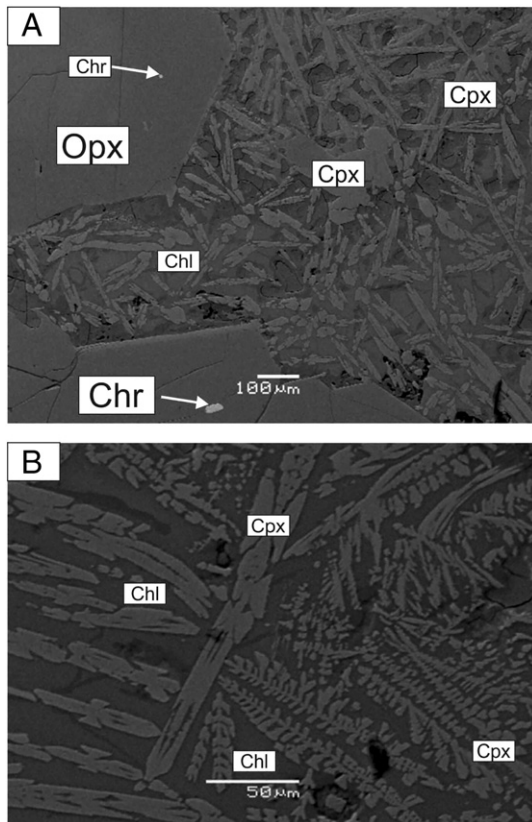
Fig. 5. Back-scattered electron (BSE) images (A, B) from high-Mg basaltic dyke from the Pournari area, showing skeletal form (spinifex) and branching growth of clinopyroxenes between large crystals of orthopyroxenes (Opx) in a chlorite-dominated matrix.

Occasionally, the silicate inclusions in chromite contain S (ranging from 0.34 to 0.83 wt% as SO_3), due probably to very fine (<2 μm) sulfide globules (Fig. 4A–C). Microprobe analysis of the inclusions is difficult, due to their small size (<5–10 μm) and interference from host chromite, but significant contents of elements absent in chromite can be clearly associated with the inclusions, which contain Na_2O (up to 2.8 wt%), K_2O (up to 1.0 wt%), and Cl (up to 0.8 wt%).

5.2. Geochemical characteristics

5.2.1. Major and trace elements

Major and trace element data from each suite are well-clustered about mean values but their variations nonetheless show petrologically meaningful correlations among elements. In the ultramafic lavas from Agrilia, SiO_2 is low and ranges from 46.9 to 47.8 wt%, TiO_2 from 0.35 to 0.40 wt%, Al_2O_3 from 6.1 to 6.6 wt%, while the MgO is quite high and ranges from 31.1 to 32.7 wt%. Similarly, the dykes from Pournari have a limited compositional range, with SiO_2 from 53.5–54.6 wt%, TiO_2 0.21–0.26 wt%, Al_2O_3 10.7–12.5 wt%, CaO 8.5–10.2 wt% and MgO 11.5–13.7 wt%. Compatible trace elements in the Agrilia ultramafic lavas show a relatively large range in Cr from 1070 to 1900 ppm, while Ni is more uniform between 1400 to 1560 ppm. In contrast, the Pournari dykes display narrower ranges and much lower contents of compatible trace elements; Cr varies from 770 to 1060 ppm and Ni from 210 to 280 ppm.

In the IUGS classification scheme (Le Bas, 2000) a picrite or picritic basalt contains ≥12% MgO, <52% SiO_2 and >3% $Na_2O + K_2O$. According to the same scheme, for TiO_2 <1 wt%, the total alkali content is critical to discriminate between picrite and komatiite. Less than 1 wt% Na_2O + K_2O content suggests a komatiitic composition. In an Al_2O_3/TiO_2 vs. TiO_2 plot (Fig. 12), the Agrilia whole-rock compositions are within the array defined by arc ultramafics (displaying boninite-like affinities;

from Khanna et al., 2016) and picritic rocks but also within the komatiitic array; they are certainly offset from the trend defined by arc basalts. However, given recent refinement of the definition of komatiite, these criteria are not sufficient to resolve the petrologic type of the Agrilia ultramafic lavas. We discuss further in the next Section 6.1 (Classification of ultramafic lavas) how to apply defining characteristics and make a judgment about the proper assignment of a petrologic type name to these lavas.

In contrast, the major and trace element characteristics of the Pournari dykes are plainly associated with rocks of boninitic affinity. The definition of boninite calls for MgO content in the range 8–15 wt%, TiO_2 < 0.5 wt%, Ni between 70 and 450 ppm, and Cr between 200 and 1800 ppm, as observed in this case. Additionally, the Al_2O_3/TiO_2 ratio is within the expected range for rocks with boninitic affinities (Fig. 12). However, these rocks do not meet the strict definition of boninite because SiO_2 is lower than 57 wt% and the Ti/Zr ratio (78 to 180 in the Pournari dykes) is higher than in boninites (23–63). Despite these differences, the Pournari rocks do trend toward boninites.

6. Discussion

6.1. Classification of ultramafic lavas

Given a whole rock that contains a significant concentration of olivine phenocrysts, the whole rock MgO content does not reliably indicate the MgO content of a magmatic liquid. However, subject to certain assumptions, the MgO content of the liquid from which the olivine grew can be inferred from the whole rock chemistry, the composition of the olivine phenocrysts, and experimental data on Fe—Mg partitioning between olivine and liquid (e.g., Bickle, 1982). More specifically, the distribution coefficient $K_D = [(MgO)/(FeO)]_{liquid}/[(MgO)/(FeO)]_{olivine}$ is a weak function of variables such as pressure and liquid composition and hence a reliable quantity for estimating unknown liquid compositions. For olivine of the composition observed in Agrilia ultramafic lavas ($Fo_{90–94}$), K_D ~ 0.314 (Toplis, 2005). Converting this to a liquid MgO content requires solving a mass balance problem whereby olivine of composition ~Fo_{92} and liquid in equilibrium with such olivine are mixed in unknown proportions so as to yield the whole rock FeO* and MgO contents. This calculation assumes that the whole rock FeO* and MgO as measured are not too strongly affected by alteration, and that we are solving for liquid at the time olivine began to crystallize, before the appearance of clinopyroxene. Please see the appendix for a complete set of equations and method for this calculation, which was incompletely described by Bickle (1982).

If all the Fe were FeO, the resulting estimate, an upper bound among equilibrium models, would be 17 wt% MgO in the liquid and the olivine fraction in the mass balance would be ~50%, which is close to the observed modal abundance of olivine phenocrysts. However, some fraction of the total Fe in the liquid may have been in the Fe^{3+} (Fe_2O_3) state, which does not contribute to the olivine/liquid K_D calculation. Any Fe^{3+} would lower the estimates of liquid MgO and olivine mass fraction (Bickle, 1982; Economou-Eliopoulos and Paraskevopoulos, 1989). Direct constraints on the oxidation state of the Agrilia parental magma are lacking, but it is likely to have been higher than, for example, that of the Gorgona suite, assumed to have $Fe^{2+}/\Sigma Fe = 0.90$ by Herzberg et al. (2007). Recent investigations of primitive undegassed basaltic glasses and melt inclusions from a range of plate tectonic settings (Kelley and Cottrell, 2009), indicate that magmatic $Fe^{3+}/\Sigma Fe$ ratios increase toward subduction zones (back-arcs, arcs) and correlate with H_2O content and tracers of slab-derived fluids. Since the trace element contents (Table S1) and isotopic (εNd) signatures (Barth et al., 2008; Koutsovitis et al., 2012; Monjoie et al., 2008) suggest a SSZ environment for the Agrilia lavas, they are likely to have contained appreciable Fe^{3+} and hence the olivine was likely in equilibrium with liquids containing <17 wt% MgO. Furthermore, the same mass balance calculation, subtracting 44–50% Fo_{92} olivine from the whole rock compositions of
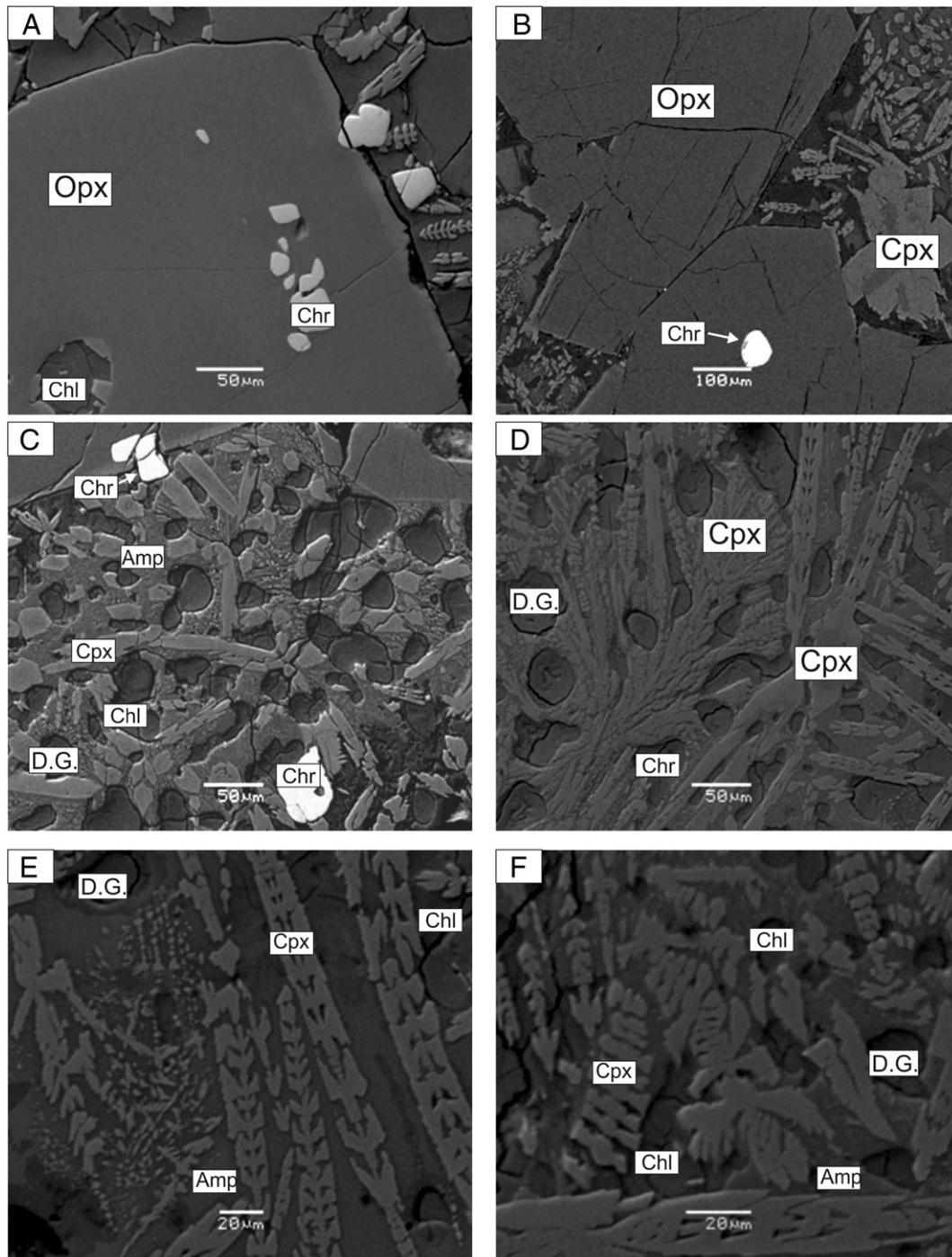
Fig. 6. Back-scattered electron (BSE) images from high-Mg basaltic dyke from the Pournari area showing (A, B) the association of chromite with orthopyroxene, (C) melt inclusion in chromite associated with clinopyroxenes in devitrified glass, (C, D) abundant amygdales of chlorite, amphibole, and very fine clinopyroxene, and (E, F) impressive branching, skeletal clinopyroxenes in a matrix of devitrified glass, amphibole and chlorite.

the Agrilia lavas, yields liquid with a mild boninitic affinity, with estimates of 52–55% SiO_2 at up to 17 wt% MgO. One exception to the claim that the derived liquid MgO content is an upper bound, though, is the possibility of disequilibrium growth that yields an artificially high K_D (Sossi and O'Neill, 2016).

The primary liquid model and fractionation conditions inferred are also compatible with the observed Ni—Fo systematics of the olivine compositions from Agrilia (Fig. 7). Although there are olivines extending up to $Fo_{93.9}$ and such magnesian olivines are commonly associated with komatiite-like liquid compositions, in fact MELTS modeling shows that the observed olivine compositions could form along a liquid

line of descent beginning with the 17% MgO liquid computed above, so long as fractionation conditions are sufficiently hydrous and oxidizing to raise the effective K_D far enough. Fig. 7 includes a curve of computed olivine compositions from a MELTS calculation at 1000 bars, fO_2 2.75 log units above QFM, sufficient H_2O to saturate the melt, and 0.1135 wt% NiO in the primary melt.

Although the definition of komatiite is debated, the previous suggestion that Agrilia rocks are komatiitic lavas (Paraskevopoulos and Economou, 1986) is not consistent with the inferred primary liquid MgO being lower than 18 wt% (Arndt et al., 2004). Even though the current whole-rock MgO contents are >30 wt% and the pre-alteration
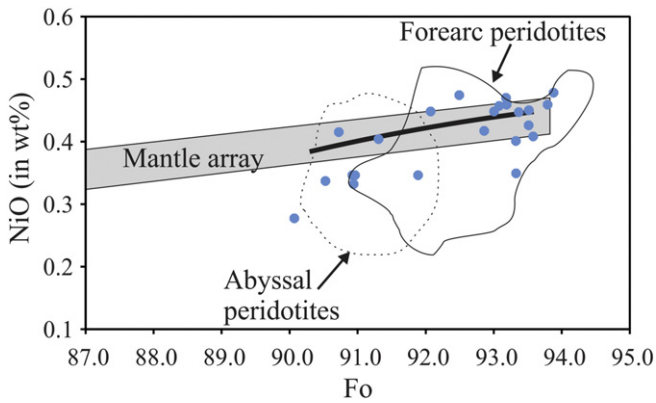
Fig. 7. Variation of Fo versus NiO (in wt%) in olivines from ultramafic lavas (Agrilia). The bold curve show best-fit olivine compositions that arise during MELTS modeling. The MELTS run shows fractional crystallization (FC) in 1 °C increments at pressure 1000 bar, fO_2 buffered to QFM + 2.75 and initial H_2O content sufficient to saturate the melt. The initial NiO content was selected at 0.1135 wt% in order to fit the highest Fo olivines. Olivine compositions for forearc (Ishii et al., 1992) and abyssal (Dick, 1989) peridotites shown as continuous and dashed field lines, respectively; mantle olivine array from Takahashi (1986).

whole rock MgO content including olivine phenocrysts was likely higher than 18 wt%, we conclude that the use of the term komatiite to describe these lavas is inconsistent with current usage; they are picrites.

6.2. From slow- to rapid-growth during crystallization of ultramafic lavas

The olivine phenocrysts in the Agrilia ultramafic lavas are generally equant and show no evidence of anomalous trace element incorporation. They are non-spinifex and display no evidence requiring that they grew at fast rates. They are likely to be pre-eruptive phenocrysts.

The clinopyroxene in the Agrilia lavas is different in character. Cpx is distinctly zoned, showing decreasing MgO content and correlated increasing Al_2O_3 and FeO contents from core to rim (Fig. 8; Table 2). These correlations are qualitatively consistent with those expected from progressive cpx growth during fractional crystallization from an evolving liquid. However, in detail the slope of MgO vs. Al_2O_3 is substantially steeper than expected from conventional fractional crystallization models in which each increment of solid grows in equilibrium with the evolving liquid composition. The most evolved compositions, with 11 wt% Al_2O_3, are highly unlikely to be equilibrium cpx compositions under low-pressure conditions. We argue that these compositions are consistent with disequilibrium growth at interface velocities that are rapid relative to mobility of Al_2O_3 in the melt (Powell et al., 1980) and that allow development of a highly Al_2O_3-enriched diffusive boundary layer at the growing crystal surface. When growth occurs at such a rate that incompatible elements such as Al cannot diffuse away from the interface as fast as needed to maintain a homogeneous liquid composition in the adjacent melt, there is excess incorporation of Al and other elements in the crystal, which in turn may modify the crystal shape and feedback into changing the crystal growth rate (Jambon et al., 1992). Depending on whether the substituting cations favor morphologies that increase or decrease surface area, this feedback can be positive or negative, but in either case the anomalous enrichment trend in cpx compositions suggests rapid and therefore probably post-eruptive growth of most of the cpx population.

Experimental relationships between the Al_2O_3 content of spinel and melt (Maurel and Maurel, 1982) have shown that the Al_2O_3 content in spinel may be used to estimate the composition of the liquids from which they grew. Maurel and Maurel (1982) give the relationship $(Al_2O_3)_{spinel} = 0.035(Al_2O_3)_{melt}^{2.42}$ (Al_2O_3 in wt%) for spinel compositions fall within the following compositional range: $TiO_2 < 2.5$ wt%, FeO* 13–60 wt%, $Cr_2O_3 > 13$ wt% and $Al_2O_3 > 4$ wt%. This component of spinel is not strongly affected by subsolidus re-equilibration with olivine or by
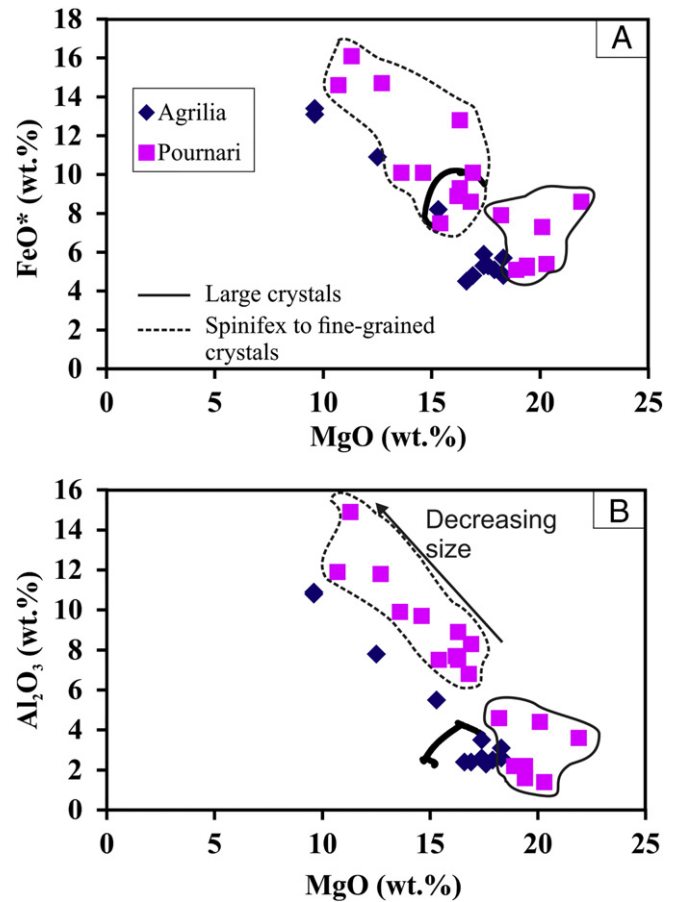

Fig. 8. Variation of (A) FeO* and (B) Al_2O_3 versus MgO in clinopyroxenes from ultramafic lavas (Agrilia) and high-Mg basaltic dykes (Pournari). The bold curves show clinopyroxene compositions that arise during equilibrium crystallization according to MELTS using the preferred fractionation conditions described in the text. The continuous and dashed outlines around subsets of the Pournari cpx data distinguish by texture the large crystals (solid outline) and spinifex to fine-grained crystals (dashed outline). The black arrow in B indicates the direction of decreasing size for the spinifex to fine-grained crystals.

postcumulus reactions (Pagé and Barnes, 2009). For the Agrilia sequence, the calculated Al_2O_3 content of the melts (Fig. 9) in equilibrium with the chromite are 8.5–9.0 wt% for chromite inclusions within olivine, 8.3–9.2 wt% for the chromite inclusions in clinopyroxene, and 8.0–9.2 wt% for matrix chromite. The effectively constant or gently increasing melt Al_2O_3 contents are consistent with the absence of plagioclase as a fractionating phase.

The textural and compositional evidence from the Agrilia lavas suggest that non-spinifex cumulate olivine phenocrysts and associated Ti-poor chromite may have been formed during a pre-eruptive stage of magma crystallization, followed by transport, eruption, and crystallization of clinopyroxene, amphibole (subsequently decomposed to rhönite), and Ti-magnetite in the matrix of the rapidly cooling ultramafic lava (Figs. 3, 4).

6.3. Implications based on Rhönite from Agrilia lavas

Rhönite, although uncommon, has been observed in a variety of rock types. In alkaline, Si-undersaturated mafic to intermediate lavas (Grapes and Keller, 2010) it occurs as phenocrysts, in groundmass (coexisting with augite and magnetite), and as inclusions in olivine. In basalts, it can be associated with complete or partial alteration of kaersutite or in basaltic scoria as daughter crystals within melt

Table 2
Major-element composition (wt%) of clinopyroxenes determined by EPMA from the Othris ophiolite complex.

	Agrilia							Pournari					
	Large crystals					core	rim	Large crystals					
Sample	A34b							LM16.2					
SiO2	53.4	54.2	52.8	53.3	50.6	54.1	43.3	52.4	54.5	54.3	53.5	53.4	53.9
TiO2	0.4	0.5	0.2	0.5	0.9	n.d.	1.2	n.d.	n.d.	n.d.	n.d.	n.d.	n.d.
Al2O3	2.4	2.9	2.6	2.5	5.5	1.2	11.3	2.9	1.4	1.6	2.2	2.2	1.8
FeO	5.1	4.8	5.7	5.1	8.2	5.3	13.3	6.3	5.4	5.2	5.3	5.1	5.2
MgO	17.2	18.3	18.3	17.9	15.3	19.8	9.3	18.1	20.3	19.4	19.4	18.9	19.1
CaO	21.2	20.1	20.7	20.5	19.6	19.1	19.8	19.3	17.6	19.5	17.7	18.8	19.2
Cr2O3	0.4	0.8	0.4	0.3	n.d.	0.4	n.d.	0.4	0.6	0.4	0.9	0.8	0.8
Total	100.1	101.6	100.7	100.1	100.1	99.9	98.2	99.4	99.8	100.4	99.0	99.3	100.0
Mg#	0.86	0.87	0.85	0.87	0.77	0.87	0.55	0.83	0.87	0.87	0.86	0.87	0.87
	Pournari Spinifex crystals												
Sample	LM16.2												
SiO2	50.7	50.6	50.2	51.1	51.1	48.6	47.8	46.6	49.4	47.1	48.7	49.7	50.8
TiO2	n.d.	n.d.	0.3	n.d.	n.d.	0.4	0.3	0.4	0.3	0.4	0.3	0.4	0.3
Al2O3	6.8	8.3	7.7	7.5	6.2	7.6	10.4	10.6	11.6	11.9	8.8	8.9	13.6
FeO	8.6	10.1	8.9	7.5	9.1	9.3	9.4	11.3	14.4	14.6	12.3	12.8	14.9
MgO	16.8	16.9	16.3	15.4	17.9	14.7	13.5	12.8	12.6	10.7	14.9	16.3	11.5
CaO	16.8	14.2	16.6	18.8	13.9	18.4	18.1	17.4	13.4	14.1	14.6	12.1	8.1
Cr2O3	n.d.	n.d.	n.d.	n.d.	n.d.	n.d.	n.d.	n.d.	n.d.	n.d.	n.d.	n.d.	n.d.
Total	99.7	100.1	100.0	100.3	98.2	99.0	99.5	99.1	101.7	98.8	99.4	100.2	99.2
Mg#	0.78	0.75	0.76	0.78	0.78	0.74	0.72	0.67	0.61	0.57	0.68	0.7	0.57

n.d.: not determined
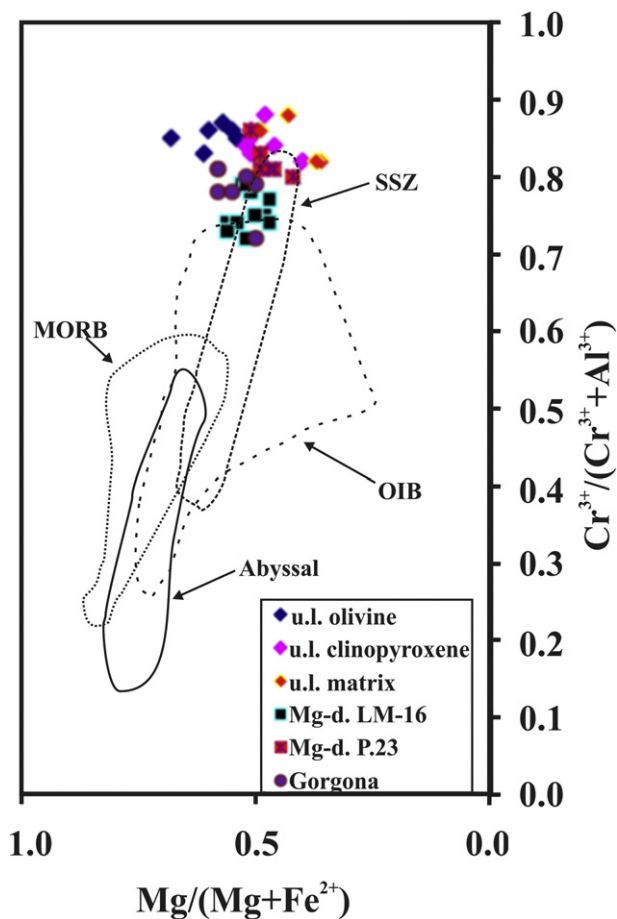
Fig. 9. Compositional variation of Cr# [(Cr^{3+}/(Cr^{3+}+Al^{3+})] versus Mg# [(Mg/(Mg + Fe^{2+})] of chromites in the Agrilia and Pournari areas of the Othris ophiolite complex. Data from Table 1 and Gorgona komatiites (Echeverria, 1980). Symbols: u.l. = ultramafic lavas; Mg-d = Mg-rich dykes.

inclusions (e.g., Jannot et al., 2005). In kimberlites, rhönite is found as inclusion in diamonds. In meteorites, it occurs in calcium-aluminum-rich inclusions in carbonaceous chondrites and angrites, in lunar meteorites as inclusions in augite, and in ureilites as inclusions in Cr-poor spinel-like phases (e.g., Treiman, 2008; Warren et al., 2006). Iron-rich rhönite (25–28 wt% FeO$_{total}$) has been described both as a late crystallizing phase, in the Kaiserstuhl volcanic complex (Grapes and Keller, 2010), and as an early crystallizing phase, in olivine-hosted melt inclusions with Mg# >0.5 from alkali basalts in Israel (Sharygin et al., 2011; Fe^{2+} estimated after Kunzmann, 1999). Experimentally, rhönite stability may extend to at least 1320 °C. At more moderate temperatures, between 1150 and 1250 °C (Boivin, 1980; Grandclément, 1980), it is observed over a wide range of fO$_2$, between the iron-wüstite (IW) and hematite-magnetite (HM) buffers (Kunzmann, 1999). Nevertheless, rhönite in olivine inclusions has been assigned to growth over a narrow temperature range (1180–1260 °C) and at pressure <500 bar (Sharygin et al., 2011). Given enough H$_2$O to saturate the liquid, magmatic growth of rhönite may extend as low as 1000 °C (Huckenholz et al., 1988), and conditions for joint crystallization of amphibole and the associated rhönite are constrained to a narrow range of pressure and temperature (200–500 bar and 1000–1050 °C). Shaw (2009) showed in 1 atm experiments that partial (at 1050 °C) or complete at (1100 °C) decomposition of kaersutite yields an assemblage of rhönite + clinopyroxene + glass + Fe-Ti oxide with a distinctive acicular shape of clinopyroxene and rhönite crystals oriented parallel to the elongation of the original amphibole.

To our knowledge, the Othris locality is the first reported occurrence of rhönite in a picritic lava. The presence of rhönite in chromite-hosted inclusions, in association with Ti-magnetite (Figs. 3, 4; Tables 3, 4) in devitrified glass, and intergrown with amphibole (Fig. 4d, f) suggests formation at multiple stages during evolution of the magma. Rhönite in chromite-hosted melt inclusions may be a primary igneous phase, but the others likely reflect Ti-rich amphibole decomposition events. Although relict kaersutite is absent, rhönite occurs in an assemblage of tschermakitic amphibole + Ti-Magnetite + glass (now devitrified) + clinopyroxene (Fig. 3D). Texturally, the secondary tschermakitic amphibole and rhönite both display acicular shapes with common orientations (see Fig. 3F,H) intersecting at ~60°, presumably controlled by the orientation of the original kaersutite. The absence of any relict

Table 3
Major-element composition (wt%) of chromite (Chr) and Ti-magnetite (Ti-Mt) determined by EPMA from Agrilia and Pournari areas.

	Agrilia												
	Chr within Ol						Chr inclusions within Cpx						
Sample	A34b												
SiO2	n.d.	0.4	n.d.	0.3	0.4	0.5	n.d.	n.d.	n.d.	n.d.	n.d.	n.d.	n.d.
TiO2	n.d.	0.3	0.25	n.d.	0.25	0.2	0.2	0.34	n.d.	0.5	0.2	0.22	0.22
Al2O3	7.1	6.4	6.8	6.5	6.3	6.7	6.8	7.6	7.1	7.5	5.9	7.4	6.7
Cr2O3	62.2	59.6	58.6	59.1	60.8	57.8	58.2	53.6	56.1	56.1	59.9	57.8	59.2
Fe2O3	3.6	7.1	8.8	7.8	5.9	6.4	7.2	9.1	9.2	7.7	5.1	7.1	6.4
FeO	16.2	14.3	11.8	14.1	15.4	16.8	17.2	21.1	19.7	17.6	18.3	17.3	17.3
MnO	0.4	n.d.	n.d.	0.4	0.3	n.d.	n.d.	0.64	n.d.	n.d.	n.d.	n.d.	0.6
MgO	11.2	12.1	13.8	12.4	11.4	10.9	10.3	8.1	8.6	10.4	9.5	10.3	10.2
NiO	n.d.	n.d.	n.d.	n.d.	n.d.	n.d.	n.d.	n.d.	n.d.	n.d.	n.d.	n.d.	n.d.
Total	100.7	99.9	100.1	100.3	100.7	99.3	99.7	100.5	100.7	99.8	98.8	100.1	100.6
Cr#	0.86	0.86	0.85	0.83	0.87	0.85	0.85	0.82	0.84	0.83	0.88	0.84	0.86
Mg#	0.55	0.6	0.68	0.61	0.57	0.54	0.51	0.4	0.46	0.51	0.48	0.52	0.51

	Agrilia					Pournari							
	Chr within matrix				Ti-Mt	Small inclusions within Cpx (LM 16)						Matrix P.23	
Sample	A34b					LM16.2							
SiO2	n.d	n.d.	n.d.	0.4	0.8	n.d.	n.d.	n.d.	0.4	n.d.	n.d.	n.d.	n.d.
TiO2	0.27	0.5	0.3	0.2	4.6	0.2	n.d.	n.d.	0.2	n.d.	0.2	n.d.	n.d.
Al2O3	5.4	7.6	6.4	6.8	7.6	11.8	13.8	10.1	12.9	10.1	11.8	9.9	8.9
Cr2O3	59.2	50.5	60.5	57.8	1.4	51.2	51.9	55.1	51.1	56.6	53.1	58.4	55.8
Fe2O3	6.5	11.3	5.1	6.8	51.4	8.1	5.8	6.7	7.8	5.4	6.4	4.1	6.9
FeO	20.1	22.6	18.1	16.5	31.0	19.1	17.6	17.4	16.3	17.1	18.6	18.9	18.2
MnO	n.d	n.d.	n.d.	n.d.	0.3	n.d.	n.d.	n.d.	n.d.	0.6	n.d.	n.d.	n.d.
MgO	8.5	7.1	9.7	10.9	3.6	9.6	10.8	10.6	11.6	10.8	9.98	9.5	9.8
NiO	n.d	n.d.	n.d.	n.d.	n.d.	n.d.	n.d.	n.d	n.d.	n.d.	n.d.	n.d.	n.d.
Total	100.0	99.6	100.1	99.4	100.7	100	99.9	99.9	100.3	100.6	99.9	100.8	99.6
Cr#	0.88	0.82	0.86	0.85	0.11	0.74	0.72	0.79	0.73	0.79	0.75	0.81	0.82
Mg#	0.43	0.36	0.49	0.54	0.17	0.47	0.52	0.52	0.56	0.53	0.49	0.47	0.49

kaersutite implies that temperature after decompression was high enough (~1100 °C) to fully decompose it, but formation of secondary tschermakitic amphibole in addition to clinopyroxene suggests partial pressure of H_2O higher than that in Shaw's experiments and hence total pressure above 1 bar and non-zero H_2O activity. The absence of preserved glass from these areas and the small size of the crystals makes it difficult to reconstruct the original amphibole composition by mass balance calculations, but qualitatively it may have been similar to the starting material used Shaw (2009).

In the Agrilia lavas, the rhönite-bearing areas formed after kaersutitic amphibole generally have high Al_2O_3 contents and suggest that growth of primary kaersutite may have contributed to the slight decrease during fractionation in liquid Al_2O_3 contents despite the absence of plagioclase fractionation. The decrease in Al_2O_3, though resolvable from spinel chemistry, is weak enough that the disequilibrium Al_2O_3 enrichment in rapidly grown cpx can overwhelm it and preserve a negative correlation between MgO and Al_2O_3 in cpx.

6.4. Fractionation sequence of high-Mg dykes

Mineral texture and chemistry in the Pournari samples provides targets for quantitative models of the evolution of the dyke-forming magmas. Orthopyroxene appears to be the liquidus phase and to predate rapid quench along dyke margins. Clinopyroxene shows intercrystalline trends of decreasing MgO content and correlated increasing Al_2O_3 and FeO contents from the large crystals, through smaller spinifex-textured crystals, and continuing to the fine crystals (Fig. 8; Table 2). The spinel chemistry approach of Maurel and Maurel (1982) applied to the Pournari chromite implies a range in melt Al_2O_3 content from 10.39 to 11.82 wt% for equilibrium with chromite inclusions in cpx (sample LM16) down to 9.86 to 10.30 wt% in equilibrium with matrix chromite (sample P23). The significant decrease in Al_2O_3 suggests fractionation of an Al_2O_3-rich phase.

The fractional crystallization of the Pournari dykes was investigated using the MELTS model (Ghiorso and Sack, 1995), as implemented in the alphaMELTS interface (http://magmasource.caltech.edu; Smith and Asimow, 2005). The whole-rock compositions were used, which evidently neglects possible changes in bulk composition due to alteration and weathering, but the models are evaluated on the basis of mineral chemistry and phase sequence constraints, which are robustly preserved features of the rocks. Across a substantial range of pressure (500–2000 bar), oxygen fugacity (fO_2, varied from the Quartz Fayalite Magnetite (QFM) buffer to 2.5 log units above QFM), and magmatic H_2O (0 to 1.5 wt%) conditions, orthopyroxene and chromite are consistently the first two phases to form near the liquidus. Above 2 wt% H_2O, the liquidus phase changes to olivine, which is not consistent with petrographic observations. There is also a lower bound on H_2O content from the absence of plagioclase in the rock, which requires at least 0.3 wt% H_2O in the primary melt, At least in the case of sample P23, according to the modeled compositions, the Al_2O_3 in the liquid at the appearance of chromite is 11.06 wt%. The next phase to appear is always a clinopyroxene. The composition of this clinopyroxene, however, is sensitive to fO_2. If conditions are too reducing or pressure too high then the FeO in the liquid stabilizes pigeonite, which is not observed in any of the samples. Thus, the predicted MELTS conditions are in accord with the observed mineralogical data if crystallization occurred at pressure <1000 bar and oxygen fugacity at least 1.6 log units higher than the QFM buffer; both these conditions are required to stabilize only augite and suppress pigeonite until low enough temperatures that it would not appear before quench. An assemblage of opx and chromite would have formed by slow cooling at temperatures between the liquidus (1296 °C with 0.5 wt% initial H_2O; 1318 °C with 0.3 wt% initial H_2O) and ~1190 °C, followed by the onset of rapid cooling. Based on the presence of dendritic augite, which appears on the liquidus at 1188 °C with 0.3 wt% H_2O and at 1163 °C with 0.5 wt% H_2O, and the absence of coarse plagioclase, which appears on the liquidus at 1133 °C with 0.5 wt% H_2O and at 1160 °C with 0.3 wt% H_2O, we divide the rapid
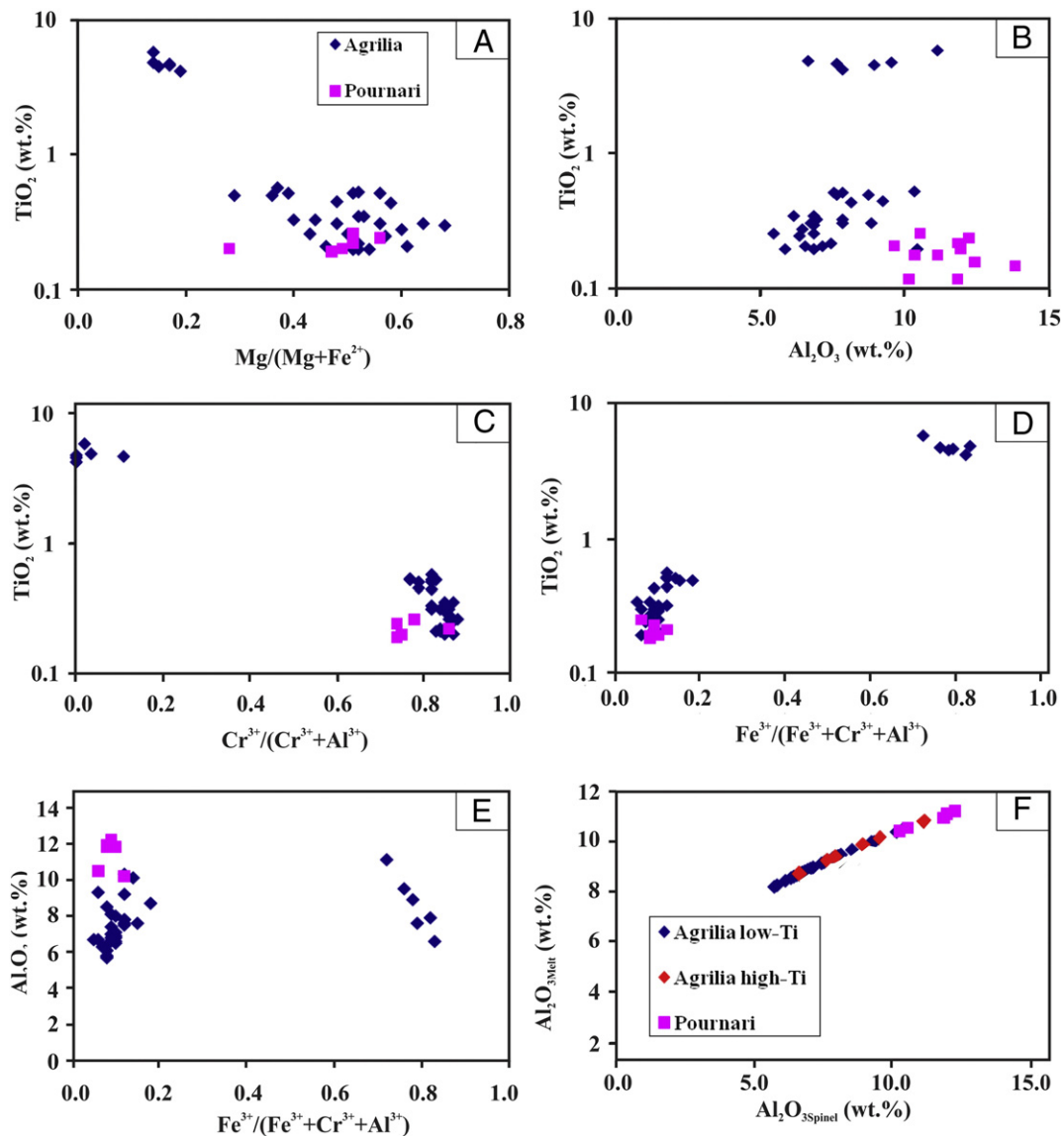
Fig. 10. Spinel chemistry from the studied samples: variation of TiO_2 versus (A) $Mg/(Mg + Fe^{2+})$, (B) Al_2O_3 content, (C) $Cr^{3+}/(Cr^{3+}+Al^{3+})$, and (D) $Fe^{3+}/(Cr^{3+}+Al^{3+}+Fe^{3+})$. (E) Al_2O_3 content versus $Fe^{3+}/(Cr^{3+}+Al^{3+}+Fe^{3+})$ ratio. (F) Calculated Al_2O_3 content in the melt (using the equation proposed by Maurel and Maurel, 1982) versus Al_2O_3 content in spinel. Symbols for A–E as in Fig. 7.

cooling stage into a phase slow enough to allow some dendritic crystal growth at 50–75 °C undercooling relative to cpx-in, followed by a genuine quench phase forming glass (now devitrified) from the remaining liquid, before significant nucleation or growth of plagioclase (Fig. 13). An alternative explanation would allow for differences in nucleation and growth kinetics between augite and plagioclase, in which case there may not have been a change in cooling rate or glass transition between ~1150 and ~1100 °C.

As discussed above for the Agrilia clinopyroxene compositions, the parallel trends of Al_2O_3 and FeO^* enrichment with decreasing MgO in the Pournari cpx grains is only qualitatively consistent with the standard model of fractional crystallization. The enriched end of these correlations, reaching 16 wt% FeO^* and 15 wt% Al_2O_3, does not occur in any local equilibrium model of crystal growth in which each increment of crystal growth occurs in equilibrium with the evolving liquid. Rather, the anomalous rate of Al_2O_3 enrichment reflects an interval of large undercooling during which major elements like Al_2O_3 were far from equilibrium (Shea et al., 2015). The steep enrichment of Al_2O_3 requires a true disequilibrium model, in which growth rates are faster than the transport of incompatible Al_2O_3 components away

from the growing crystal. In such a scenario, an Al_2O_3-enriched diffusive boundary layer grows at the crystal surface and Al_2O_3 concentrations in cpx can eventually exceed, locally, those in the far-field melt pool. This is entirely consistent with the growth rates experimentally inferred for development of dendritic, micro-spinifex textured cpx (Walker et al., 1976). In particular, the snow-plow effect should have operated at the boundaries of the growing cpx grains. Even though Al is an incompatible component in cpx, at these growth rates, the Al is incorporated into cpx from such an enriched boundary layer that it acts compatibly compared to the far-field liquid and can constitute the Al-fractionating phase necessary to explain the apparent decrease in liquid Al_2O_3 witnessed by the spinel chemistry.

6.5. Implications for rapid growth

Although spinifex textures are sometimes considered to be unique to komatiite flows, there is a growing recognition that similar textures can also be formed in high-level dykes and sills (Arndt et al., 2008). Two processes may promote the formation of spinifex texture: quench crystallization in liquids that become highly super-cooled as a result of

Table 4
Major-element composition (wt%) of inclusions in Chr and d.G. determined by EPMA from Agrilia area (sample A34b).

	d.G.					d.G.		
	Rho					Amph		
SiO_2	25.6	27.3	25.8	26.3	26.6	39.8	40.4	40.6
TiO_2	3.7	4.2	4.7	4.9	3.9	1.9	1.2	0.73
Al_2O_3	17.5	15.6	15.2	15.7	14.9	16.5	17.5	15.2
Cr_2O_3	n.d.	n.d.	n.d.	n.d.	n.d.	n.d.	n.d.	n.d.
FeO	27.4	27.6	30.3	28.9	29.8	17.7	17.1	17.8
MnO	n.d.	n.d.	0.3	0.2	0.2	n.d.	0.3	0.3
MgO	8.2	8.6	8.8	8.8	8.7	9.2	10.6	9.7
CaO	10.2	9.1	10.6	10.7	10.6	10.1	9.6	9.23
Na_2O	0.5	0.8	1.3	0.5	0.5	2.5	1.7	1.4
K_2O	n.d.	0.4	n.d.	n.d.	n.d.	0.3	0.2	n.d.
NiO	n.d.	n.d.	n.d.	n.d.	n.d.	n.d.	n.d.	n.d.
Cl	n.d.	n.d.	n.d.	n.d.	n.d.	0.2	0.2	n.d.
Total	93.1	93.6	97.0	96.0	95.2	98.2	98.8	95
Mg#	0.34	0.36	0.33	0.35	0.34	0.48	0.52	0.49

Host	Chr-Ol (Fig. 4b)			Chr (d.G.)				Cpx (d.G.)
	d.G.	Cpx	Amph	Amph	Amph	Rho	Amph	Ap
SiO_2	45.6	51.8	55.2	35.9	49.1	33.1	41.1	0.4
TiO_2	0.2	0.4	0.2	2.5	0.9	1.6	1.9	n.d.
Al_2O_3	9.9	8.5	10.6	7.7	9.0	12.1	16.4	n.d.
Cr_2O_3	1.1	1.9	1.3	0.35	4.0	0.8	n.d.	n.d.
FeO	21.8	4.6	6.2	17.1	5.8	27.1	16.1	2.1
MnO	0.2	n.d.	n.d.	0.2	n.d.	0.2	n.d.	n.d.
MgO	6.5	18.8	11.1	27.2	12.6	14.5	11.3	n.d.
CaO	3.1	9.8	10.4	1.6	16.7	4.3	10.3	51.2
Na_2O	6.9	2.8	2.7	2.6	1.3	1.6	1.5	n.d.
K_2O	0.9	n.d.	0.3	1.0	0.2	0.2	n.d.	n.d.
P_2O_5	n.d.	n.d.	n.d.	n	n.d.	n.d.	n.d.	41.5
NiO	n.d.	n.d.	n.d.	0.3	n.d.	n.d.	n.d.	n.d.
Cl	n.d.	n.d.	n.d.	0.5	n.d.	n.d.	0.3	1.8
Total	96.2	96.6	98.0	97.0	99.6	95.5	98.9	97.0
Mg#	0.35	0.87	0.76	0.74	0.8	0.49	0.54	

Fig. 12. TiO_2 versus Al_2O_3/TiO_2 relations for the Agrilia ultramafic lavas and the high-Mg Pournari dykes. The Othris rocks are compared with Phanerozoic boninites (926 analyses acquired from the following databases: EarthChem www.earthchem.org, PetDB www.earthchem.org/petdb and Georoc http://georoc.mpch-mainz.gwdg.de/georoc/), and published data for picrites (Eggins, 1993), arc basalts (Khanna et al., 2016) and arc ultramafics (Khanna et al., 2016).

The parallel enrichment trends from core-to-rim in Agrilia cpx and from spinifex down to fine matrix cpx in Pournari samples are both consistent with the rapid cooling rates. In particular, experimental study of a lunar picrite composition (Apollo sample 12002) produced high-Al pyroxenes with skeletal textures like those in Pournari, when grown at cooling rate between 11 and 57 °C/h (Figs. 4 and 6 in Walker et al., 1976). Recent experiments by Welsch et al. (2016) suggest rapid

volatile loss or rapid growth of skeletal crystals in undegassed hydrous magmas (Grove et al., 1996). We observe a well-developed skeletal, plumose (micro-spinifex) texture in clinopyroxene between large crystals of orthopyroxene in the marginal parts of the Pournari high-Mg dykes (Figs. 5, 6). This texture, like macro-spinifex, is probably related to rapid cooling of hydrous basaltic magma (Bouquain et al., 2014). By comparison, clinopyroxene grown under equilibrium conditions, as in previous experiments undertaken to determine liquidus phase relations, have low Al contents, like the cpx cores in the present samples (Table 2).
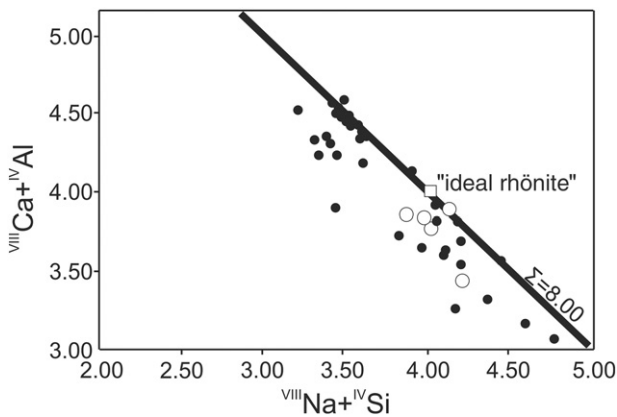

Fig. 13. MELTS model results for the fractionating mineral assemblage and mineral compositions plotted against decreasing model temperature for Pournari sample P23. The MELTS run shows fractional crystallization (FC) in 1 °C increments at pressure 500 bar, fO_2 buffered to QFM + 2.0 and initial H_2O content 0.5 wt%. The top of each bar shows the temperature when that phase appears, labeled by the composition of that phase when it begins to crystallize. There is a hiatus in orthopyroxene (Opx) crystallization when clinopyroxene (Cpx) comes in, but then Opx returns about 25 °C later. Otherwise, each phase continues to fractionate until the low-temperature end of the calculation; the bottoms of the bars are labeled by the last mineral composition predicted at the minimum temperature. For the justification for this particular fractionation condition as a model for Pournari, see text. Mineral compositions are given in terms of the parameters $Cr\# = Cr^{3+}/(Cr^{3+}+2Ti + Al^{3+})\cdot100$, $Ti\# = 2Ti/Cr^{3+}+2Ti + Al^{3+})\cdot100$, $Wo = Ca/(Ca + Mg + Fe)\cdot100$ and $En = Mg/(Ca + Mg + Fe^{2+})\cdot100$, and $An = Ca/(Ca + Na)\cdot100$. The inset represents our interpretation of the crystallization sequence and rate based on petrographic and mineral zoning observations, where we have assigned temperatures to the rate changes based on the MELTS results for onset of Cpx and plagioclase crystallization.

Fig. 11. Compositional variation of $^{VIII}Na + {}^{IV}Si$ versus $^{VIII}Ca + {}^{IV}Al$ of rhönite from Agrilia sample. The Agrilia rhönites plot below total cations per formula unit $\Sigma = 8.00$, due to the presence of ferric iron in tetrahedral coordination. Symbols: white circles: Agrilia rhönites; black circles: rhönites from Grapes et al. (2003); white square: "ideal" rhönite.
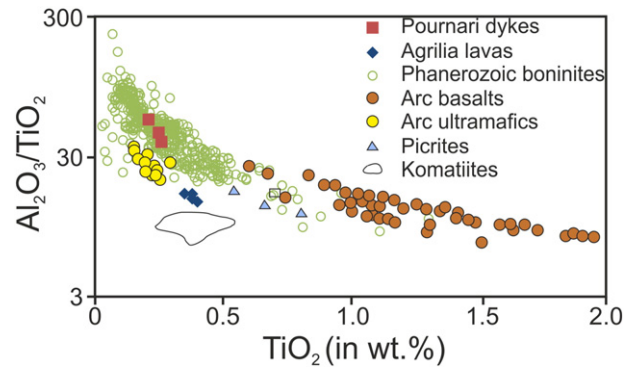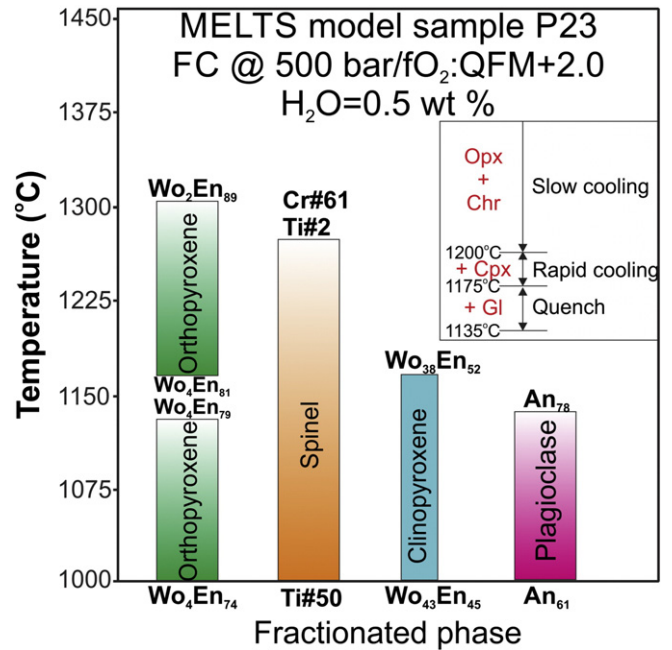
interface motion, on the order of 10^{-6} m/s, for the formation of cpx crystals with dendritic shapes. Furthermore, they suggest that growth rate is extraordinarily sensitive to degree of undercooling or supersaturation, increasing by three orders of magnitude between 45 °C and 55 °C below the liquidus temperature. Furthermore, the observation of Kouchi et al. (1983) suggest that sector zoning evolves toward compound zoning with decreasing degree of supersaturation. Initially skeletal or spinifex crystals grown at high supersaturation become more equant by backfilling of internal crystal voids if growth continues toward equilibrium. Only in a few cases have the dendritic cpx crystals been back-filled and the dendritic shape hidden (Figs. 5B, 6E), suggesting that degree of supersaturation, beginning at 45–55 °C, remained above 30 ± 5 °C until quench.

Another important factor controlling the texture formed during cooling of a lava or dyke is the position relative to flow top or dyke wall, which determines both the cooling rate and the local thermal gradient (Faure et al., 2006). In the uppermost layers of a lava flow or the most marginal part of a dyke, it is expected that growth patterns are dominated by the high cooling rate rather than by the thermal gradient. On the other hand, the thermal gradient becomes the dominant influence deeper in a flow and farther from a dyke wall, in the region that displays large crystals systematically oriented perpendicular to flow tops or dyke margins. In the Pournari dyke chilled margin, we observe random micro-spinifex textured cpx, not systematically oriented cpx blades. In this region, where we have inferred a cooling rate of ~50 °C/h, we would expect oriented crystal growth in a

thermal gradient exceeding about 40–50 °C/cm (Fig. 19 in Faure et al., 2006). The plumose clinopyroxene texture is more consistent with lower thermal gradients in the chilled margin region, ≤30 °C/cm.

The growth of dendritic but randomly oriented cpx crystals, as observed near the boundaries of the Pournari dyke, appears to place simultaneous constraints on both cooling rate (a lower bound, ≥50 °C/h) and thermal gradient (an upper bound, ≤30 °C/cm). Hence, we applied a simple analytic model of the conductive cooling of a dyke to assess whether these two constraints can be satisfied simultaneously. We used the analytic solution from Carslaw and Jaeger (1959) for an infinite domain containing a hot slab with sharp edges at t = 0, i.e. the initial condition is $T = T_{in}$ for $-a \le x \le a$ and $T = T_{ff}$ elsewhere. To use the analytical solution, the thermal diffusivity must be taken as constant; we chose a value typical of basaltic liquid at 1200 °C, 1.6×10^{-6} m^2/s. Clearly, this simple model neglects important aspects of the problem, including latent heat, advection along and across the dyke, and variations in thermal diffusivity. However, for the near-liquidus interval during which the dendritic cpx grew, these are reasonable approximations to get a general intuition for whether the constraints are reasonable. We assumed a full dyke-width $2a$ of 1 m, comparable to that observed in the field. For liquidus temperature $T_{in} = 1350$ °C and far-field temperature $T_{ff} = 700$ °C, the progress of the solution is shown in Fig. 14 (as T vs. x, $\partial T/\partial t$ vs. x, $\partial T/\partial x$ vs. x, and $\partial T/\partial t$ vs. $\partial T/\partial x$). The boundary layer experiencing significant cooling and thermal gradients during the selected time range is restricted to the outer 10 cm of the dyke. The peak in cooling rate is 50 °C/h, at a point 4.5 cm from the
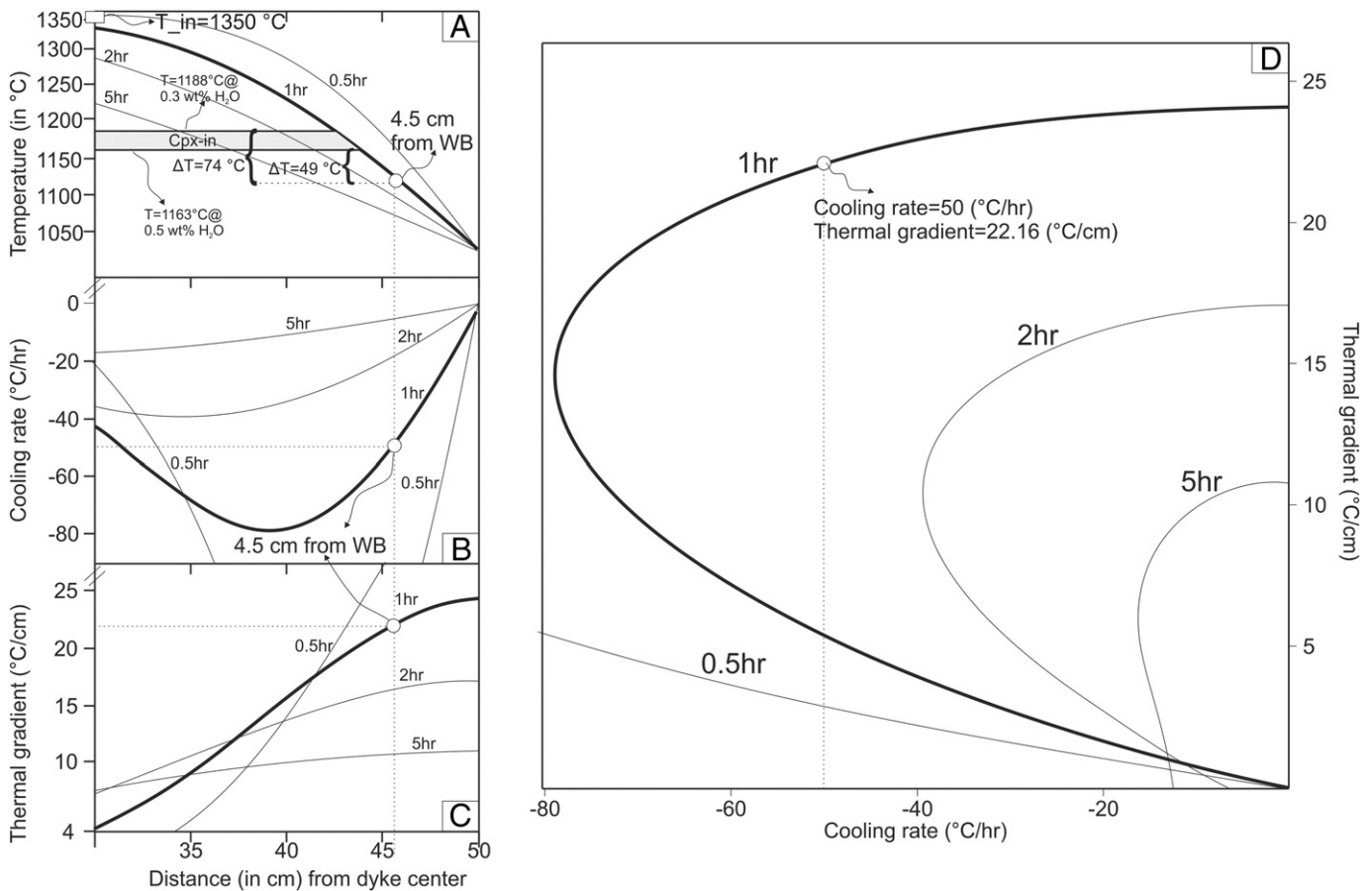

Fig. 14. Thermal model showing the conductive cooling of a 1 m dyke from Pournari area based on Carslaw and Jaeger (1959) equations for an infinite domain initially containing a one-dimensional hot slab. The wall boundary (WB) shown is at $x = +50$ cm. Distance is plotted versus temperature (A), cooling rate (B) and thermal gradient (C). The temperatures of equilibrium appearance of clinopyroxene in MELTS models and the undercooling relative to these temperatures are shown in (A). The peak cooling rate is observed at $x = 46.6$ cm, i.e. 3.4 cm from the WB. In (D) the cooling rate (°C/h) is plotted versus thermal gradient (°C/cm) to show that simultaneous constraints on these variables are satisfied at 48 °C/h and 22 °C/cm, respectively. The thick black lines correspond to model solution at t = 1 h. The thin black lines correspond to 0.5 h, 2.0 h and 5.0 h. The calculations were performed at the following conditions: dyke width: 1 m, thermal diffusivity κ: 1.6×10^{-6} m^2/s (for a basaltic liquid at temperature 1200 °C), liquidus temperature $T_{in} = 1350$ °C and far-field temperature $T_{ff} = 900$ °C.

boundary and, at the same point in space and time, the calculated thermal gradient is 22 °C/cm. This location in the model is undercooled by about 50 °C relative to the appearance of cpx on the equilibrium liquidus, a likely level of supersaturation for rapid growth and limited nucleation of cpx crystals. We conclude that randomly oriented dendritic cpx growth within a few cm of the wall of a 1 m wide basaltic dyke is quite plausible.

7. Conclusions

We present petrographic and geochemical observations of two rock types found within the crustal section of the Othris ophiolite complex: ultramafic lavas from Agrilia and high-Mg basaltic dykes from Pournari. The Agrilia lavas consist of over 50 vol% olivine phenocrysts with a random orientation. We infer an upper bound on the liquid MgO content of 17 wt%. The cumulate olivine phenocrysts and associated Ti-poor chromite in the Agrilia ultramafic lavas were probably formed during a pre-eruptive stage of magma crystallization, followed by transportation, eruption, and rapid crystallization of anomalously zoned clinopyroxene, amphibole (subsequently decomposed to rhönite), and Ti-magnetite in the matrix of the cooling lava. Furthermore, melt inclusions hosted in chromite revealed the presence of microcrystalline aggregates consisting of rhönite, clinopyroxene, amphibole, apatite, serpentine, chlorite and sometimes very fine (<2 μm) sulfide globules.

The Pournari high-Mg dykes display impressive thin-section scale micro-spinifex textures that are restricted to the dyke margins. The nucleation and crystallization of plumose, skeletal clinopyroxene with anomalous enrichment in Al_2O_3 and FeO* requires rapid cooling of hydrous basaltic magma. The random orientation of the skeletal cpx grains suggests dominant control by rapid cooling rather than growth in a thermal gradient. Finally, modeling the liquid line of descent and phase assemblages appearing in the Pournari dykes requires significant magmatic water contents (at least 0.3 wt% H_2O), oxidizing conditions (at least 1.6 log units above the QFM buffer), and low pressure (<1000 bar) at the location of dyke emplacement.

Supplementary data to this article can be found online at http://dx.doi.org/10.1016/j.lithos.2017.07.015.

Acknowledgements

Appendix A

A.1. Trace elements: method, data and implications

A.1.1. Method

PGEs (Or, Ir, Ru, Rh, Pt, Pd) and Au for the Agrilia samples were determined after pre-concentration by the nickel sulfide fire-assay to quantitatively collect all the PGE from 50-g rock samples, following the method of Hoffman et al. (1978). The nickel sulfide button was then dissolved in 12 M HCl and the residue was collected on filter paper and irradiated for 16 h alongside fluence monitor standards in the University of London reactor at Silwood Park, Ascot. Samples and standards were allowed to decay for 9 days; Os, Ru, Ir and Au were determined by decay counting; information on detection limits, precision and accuracy is given by Hoffman et al. (1978). Rh, Pd and Pt were determined by dissolution of buttons in hot aqua regia and atomic absorption spectroscopy (heated graphite atomizer) at Athens University (Department of Geology). PGE for samples from Pournari were determined by ICP-MS analysis after pre-concentration using the nickel fire assay technique from 30 g samples at Activation Laboratories, Ltd, Canada. Detection limits are Ru, Os, and Pt are 4 ppb, versus 2 ppb for Ir and Pd.

A.1.2. PGEs data

The PGE contents in the ultramafic lavas from the Agrilia Formation are uniformly low. Average PGE contents (all in ppb) are: Os = 4, Ir = 0.7, Ru = 6, Pt = 1 and Pd = 9 (Table S1; Economou-Eliopoulos and Paraskevopoulos, 1989). The Pt and Pd contents in the Pournari high-Mg basalts (8 and 28 ppb, respectively) are modestly elevated compared to the Agrilia lavas. In the Pournari suite, Ir was not detected, therefore a tentative lower bound on the Pd/Ir ratio can be estimated based on stated detection limits, 10.7 ± 3.08 (± number represents the standard error of the mean $\sigma_M = \frac{\sigma}{\sqrt{N}}$). The Ni/Cu ratio of the Pournari samples is 3.58 ± 0.31. The Agrilia samples exhibit a Pd/Ir ratio of 12.2 ± 0.39, similar to the lower bound on the same ratio in the Pournari samples, and higher Ni/Cu of 25.87 ± 1.22. In addition, the values of the Cu/Pd and Ti/Pd ratios for the Agrilia lavas are 6742 ± 291 and 26.7 × 10^3 ± 2.2 × 10^3, respectively. The Cu/Pd and Ti/Pd ratios in the Pournari high-Mg dyke samples are both lower, 3961 ± 797 and 9.1 × 10^3 ± 4.1 × 10^3, respectively.

A.1.3. Implications

The trace element evidence provided establishes several common trends between komatiites and the Othris samples, despite evidence for crystal accumulation in Agrilia (Barnes and Röeder, 2001). If we distinguish among those trace elements likely to be strongly affected by crustal contamination (Th, U, Zr, Hf, and LREE) and those trace elements less likely to reflect crustal signatures (Ta, Nb, Ti, and HREE) (Arndt and Jenner, 1986; Puchtel et al., 1997), the elevated Zr, Hf and LREE contents in the Agrilia ultramafic lavas (Table S1), as compared to typical komatiite lavas (Puchtel et al., 2013), do seem to indicate crustal contamination rather than mantle source characteristics. Furthermore, fluid alteration and/or serpentinization process may have partially mobilized elements such as Pt and Pd, but nevertheless the Pd/Ir, Ni/Cu, Cu/Pd and Ti/Pd ratios measured in the Agrilia lavas (Table S1) are all very close to those reported for typical komatiites (Barnes et al., 1988; Maier and Barnes, 2004). Similar geochemical characteristics were found in the high-Mg lavas from Pournari (Table S1). Thus, in Pt-group and compatible element signatures, the Agrilia ultramafic lavas and high-Mg basalts (Pournari) resemble young komatiitic lavas and komatiitic basalts, respectively. Focusing on those elements likely to be less affected by crustal contamination, the geochemical characteristics, mineralogical composition and mineral chemistry of the Agrilia lavas and high-Mg dykes are consistent with the tectonic setting: partial melting of a metasomatized mantle wedge, subduction, collision, and mantle-lithospheric slab interactions, during a multistage evolution and recycling of crustal materials.

A.2. Calculations of mass balance and olivine-liquid equilibrium

The method presented by Bickle (1982) to infer liquid MgO contents from olivine-phyric rocks is incomplete. We briefly present here a complete recipe for carrying out a robust mass-balance and olivine-liquid equilibrium calculation for this purpose.

The minimum amount of information needed in order to calculate the MgO_{liquid} for a whole rock that contains an unknown amount of olivine of known forsterite content in a groundmass of unknown composition includes:

1. Whole-rock FeO* (FeO^*_{WR}),
2. Whole-rock MgO (MgO_{WR})
3. Fo content of olivine (Fo)
4. K_D (using actual FeO_{liquid}, i.e. NOT the K_D' of Bickle (1982) which is based on total FeO*)

5. FeO/FeO* in the liquid (OX)

In this case, the weight FeO and MgO content of the olivine are known [defined by Fo, olivine stoichiometry, and molecular weights for MgO (MW_{FeO}) and FeO (MW_{FeO})]. Therefore, the unknowns will be the MgO_{liquid}, FeO_{liquid}, and X_{Ol} (the mass fraction of olivine in the whole rock).

The Fe-Mg mass balance equations are given by:

$$MgO_{WR} = X_{Ol} \cdot MgO_{Ol} + (1-X_{Ol}) \cdot MgO_{liquid} \qquad (1)$$

$$FeO^*_{WR} = X_{Ol} \cdot FeO_{Ol} + \frac{(1-X_{Ol}) \cdot FeO_{liquid}}{OX} \qquad (2)$$

Combining these two expressions and the definition of K_D ($MgO_{liquid}/FeO_{liquid}$)/($MgO_{Ol}/FeO_{Ol}$), we obtain the following:

$$MgO_{liquid} = G \cdot FeO_{liquid}, \text{ where } G = \frac{K_D}{\frac{MW_{FeO}}{MW_{MgO}} \cdot \left(\frac{1}{Fo-1}\right)} \qquad (3)$$

$$FeO_{liquid} = \frac{MgO_{Ol} \cdot FeO^*_{WR} - FeO_{Ol}MgO_{WR}}{G \cdot (FeO^*_{WR} - FeO_{Ol}) - \frac{MgO_{WR} - MgO_{Ol}}{OX}} \qquad (4)$$

$$X_{Ol} = \frac{MgO_{WR} - MgO_{liquid}}{MgO_{Ol} - MgO_{liquid}} \qquad (5)$$

Using Eqs. (1)–(5), we repeated the six cases given in Bickle (1982) and obtain the same answers to reasonable precision $\pm 0.1\%$ MgO_{liquid}.

In our calculation, we consider a range of possible values for: FeO/FeO* (0.8, 0.9, 1), K_D (0.304, 0.314, 0.324) and Fo (0.91, 0.915, 0.92). For sample A36, at FeO/FeO* = 1, K_D = 0.314, Fo = 0.91, we get 17.2 wt% MgO_{liquid}, 9.5 wt% FeO_{liquid}, and 47.4% olivine in the whole rock. Samples A35 and A34b in this case give 18.6 wt% MgO_{liquid} and 17.2 wt% MgO_{liquid}, respectively. The low FeO^*_{WR} in A34a leads to a lower value, 13.5 wt% MgO_{liquid}. Calculated MgO_{liquid} goes down by 1.4 wt% for each 0.1 decrease in FeO/FeO*. Calculated MgO_{liquid} goes up by 0.5 wt% for each 0.01 increase in K_D. Calculated MgO_{liquid} goes up by 1.8 wt% for each 0.05 increase in Fo of liquidus olivine. The principal of this mass balance calculation is illustrated in Fig. A1, which shows the particular case of sample A36 with FeO/FeO* = 0.9, K_D = 0.314, and Fo = 0.91 as well as giving a visual sense of the magnitude of the effects of variations in these parameters on the solution. A spreadsheet including our calculations is given as supplementary material.

References

Abbou-Kebir, K., Arai, S., Ahmed, A.H., 2015. Spinel-free dunites as a proxy to komatiitic melt activity in the mantle. Lithos 216, 315–323.
Arndt, N.T., 1986. Differentiation of komatiite flows. Journal of Petrology 27 (2), 279–301.
Arndt, N.T., 1994. Archean komatiites. Developments in Precambrian Geology 11, 11–44.
Arndt, N.T., Fleet, M.E., 1979. Stable and metastable pyroxene crystallization in layered komatiite lava flows. American Mineralogist 64, 856–864.
Arndt, N.T., Jenner, G.A., 1986. Crustally contaminated komatiites and basalts from Kambalda, Western Australia. Chemical Geology 56 (3–4), 229–255.
Arndt, N.T., Nisbet, E.G., 1982. Komatiites. George Allen and Unwin, London, pp. 1–526.
Arndt, N.T., Lesher, C.M., Houle, M.G., Lewin, E., Lacaze, Y., 2004. Intrusion and crystallization of a spinifex-textured komatiite sill in Dundonald Township, Ontario. Journal of Petrology 45 (12), 2555–2571.
Arndt, N.T., Lesher, C.M., Barnes, S.J., 2008. Komatiite. Cambridge University Press, Cambridge, UK.
Barnes, S.J., Röeder, P.L., 2001. The range of spinel compositions in terrestrial mafic and ultramafic rocks. Journal of Petrology 42, 2279–2302.
Barnes, S.J., Hill, R.E.T., Gole, M.J., 1988. The perseverance ultramafic complex, Western Australia: the product of a komatiite lava river. Journal of Petrology 29, 305–331.
Barth, M., Gluhak, T., 2009. Geochemistry and tectonic setting of mafic rocks from the Othris Ophiolite, Greece. Contributions to Mineralogy and Petrology 157, 23–40.
Barth, M.G., Mason, P.R.D., Davies, G.R., Drury, M.R., 2008. The Othris Ophiolite, Greece: a snapshot of subduction initiation at a mid-ocean ridge. Lithos 100, 234–254.
Bickle, M.J., 1982. The magnesium content of komatiitic liquids. In: Arndt, N.T., Nisbet, E.G. (Eds.), Komatiites. Allen and Unwin, London, pp. 479–494.

Bizimis, M., Salters, J.M., Bonatti, E., 2000. Trace and REE content of clinopyroxenes from supra-subduction zone peridotites. Implications for melting and enrichment processes in island arcs. Chemical Geology 165, 67–85.
Boivin, P., 1980. Donnees experimentales preliminaires sur la stabilite de la rhoinite a I atmosphere. Application aux gisements naturels. Bulletin de Mineralogie 103, 491–502.
Bouquain, S., Arndt, N.T., Faure, F., Liboure, G., 2014. An experimental study of pyroxene crystallization during rapid cooling in a thermal gradient: application to komatiites. Solid Earth 5, 641–650.
Cameron, W.E., Nisbet, E.G., 1982. Phanerozoic analogues of komatiitic basalts. In: Arndt, E.G., Nisbet, E.G. (Eds.), Komatiites. Allen and Unwin, London, pp. 29–50.
Cameron, W.E., Nisbet, E.G., Dietrich, V.J., 1979. Boninites, komatiites and ophiolitic basalts. Nature 280, 550–553.
Campbell, I.H., Arndt, N.T., 1982. Pyroxene accumulation in spinifex-textured rocks. Geological Magazine 119, 605–610.
Capedri, S., Toscani, L., Grandi, R., Venturelli, G., Papanikolaou, D., Skarpelis, N.S., 1997. Triassic volcanic rocks of some type-localities from the Hellenides. Chemie der Erde 57, 257–276.
Carslaw, H.S., Jaeger, J.C., 1959. Conduction of Heat in Solids. 2nd ed. Clarendon Press, Oxford.
Dick, H.J.B., 1989. Abyssal peridotites, very slow spreading ridges and ocean ridge magmatism. Journal of Geological Society, London, Special Publications 42, 71–105.
Dijkstra, A.H., Drury, M.R., Vissers, R.L.M., 2001. Structural petrology of plagioclase peridotites in the West Othris Mountains (Greece): melt impregnation in mantle lithosphere. Journal of Petrology 42, 5–23.
Dilek, Y., Furnes, H., 2014. Ophiolites and their origins. Elements 10 (2), 93–100.
Donaldson, C.H., 1976. An experimental investigation of olivine morphology. Contributions to Mineralogy and Petrology 57 (2), 187–213.
Dostal, J., 2008. Igneous rock associations 10. Komatiites. Geoscience Canada 35 (1).
Echeverria, L.M., 1980. Tertiary or Mesozoic komatiites from Gorgona island, Colombia: field relations and geochemistry. Contributions to Mineralogy and Petrology 73, 253–266.
Economou-Eliopoulos, M., 1996. Platinum-group element distribution in chromite ores from ophiolite complexes: implications for their exploration. Ore Geology Reviews 11, 363–381.
Economou-Eliopoulos, M., Paraskevopoulos, G., 1989. Platinum -group elements and gold in komatiitic rocks from the Agrilia Formation, Othrys ophiolite complex, Greece. Chemical Geology 77, 149–158.
Economou-Eliopoulos, M., Parry, S.J., Christidis, G., 1997. Platinum-group element (PGE) content of chromite ores from the Othrys ophiolite complex, Greece. In: Papunen (Ed.), Mineral Deposits. Balkema, Rotterdam, pp. 414–441.
Eggins, S.M., 1993. Origin and differentiation of picritic arc magmas, Ambae (Aoba), Vanuatu. Contributions to Mineralogy and Petrology 114 (1), 79–100.
Faure, F., Arndt, N.T., Libourel, G., 2006. Formation of spinifex texture in komatiites: an experimental study. Journal of Petrology 47, 1591–1610.
Garuti, G., Zaccarini, F., Economou-Eliopoulos, M., 1999. Paragenesis and composition of laurite from the chromitites of Othrys (Greece): implications for Os-Ru fractionation in ophiolitic upper mantle of the Balkan peninsula. Mineralium Deposita 34, 312–319.
Ghiorso, M.S., Sack, R.O., 1995. Chemical mass-transfer in magmatic processes. A revised and internally consistent thermodynamic model for the interpolation and extrapolation of liquid-solid equilibria in magmatic systems at elevated temperatures and pressures. Contributions to Mineralogy and Petrology 119, 197–212.
Grandclément, J., 1980. Conditions de synthèse et de stabilité de la Rhönite (Doctoral dissertation).
Grapes, R., Keller, J., 2010. Fe^{2+}-dominant rhonite in undersaturated alkaline basaltic rocks, Kaiserstuhl volcanic complex, Upper Rhine Graben, SW Germany. European Journal of Mineralogy 22, 285–292.
Grapes, R.H., Wysoczanski, R.J., Hoskin, P.W.O., 2003. Rhönite paragenesis in pyroxenite xenoliths, Mount Sidley volcano, Marie Byrd Land, West Antarctica. Mineralogical Magazine 67 (4), 639–651.
Grove, T.L., Parman, S.W., 2004. Thermal evolution of the Earth as recorded by komatiites. Earth and Planetary Science Letters 219, 173–187.
Grove, T.L., Gaetani, G.A., Parman, S., Dann, J., de Wit, M.J., 1996. Origin of spinifex textures in 3.49 Ga komatiite magmas from the Barberton Mountainl and South Africa. American Geophysical Union Transactions 77, 281.
Grove, T.L., Chaterjee, N., Parman, S.L., Medard, E., 2006. The influence of H_2O on mantle wedge melting. Earth and Planetary Science Letters 249 (1–2), 74–89.
Herzberg, C.T., O'Hara, M.J., 2002. Plume-associated ultramafic magmas of Phanerozoic age. Journal of Petrology 43, 1857–1883.
Herzberg, C., Asimow, P.D., Arndt, N., Niu, Y., Lesher, C.M., Fitton, J.G., Cheadle, M.J., Saunders, A.D., 2007. Temperatures in ambient mantle and plumes: constraints from basalts, picrites, and komatiites. Geochemistry, Geophysics, Geosystems 8, Q02006. http://dx.doi.org/10.1029/2006GC001390.
Herzberg, C., Condie, K., Korenaga, J., 2010. Thermal history of the Earth and its petrological expression. Earth and Planetary Science Letters 292 (1), 79–88.
Hoffman, E., Naldrett, A., Van Loon, J., Hancock, R.G., Manson, A., 1978. The determination of all the platinum group elements and gold in rocks and ore by neutron activation analysis after preconcentration by nickel sulfide fire assay technique on large samples. Analytica Chimica Acta 102, 157–166.
Huckenholz, H.G., Kunzmann, T., Spicker, G., 1988. Stability of titanian magnesiohastinsite and its breakdown to rhönite-bearing assemblages. Terra Cognita 8, 66.
Hynes, A.J., 1972. The geology of part of the western Othrys mountains, Greece. Unpublished Ph.D. thesis, University of Cambridge, U.K., 220 pp.
Ishii, T., Robinson, P.T., Maekawa, H., Fiske, R., 1992. 27. Petrological studies of peridotites from diapiric serpentinite seamounts in the Izu–Ogasawara–Mariana forearc, Leg

125. In: Fryer, P., Pearce, J.A., Stokking, L.B. (Eds.), Proceedings of the Ocean Drilling Program, Scientific Results, pp. 445–485.

Jambon, A., Lussiez, P., Clocchiatti, R., Weisz, J., Hernandez, J., 1992. Olivine growth rates in a tholeiitic basalt: An experimental study of melt inclusions in plagioclase. Chemical Geology 96 (3–4), 277–287.

Jannot, S., Schiano, P., Boivin, P., 2005. Melt inclusions in scoria and associated mantle xenoliths of Puy Beaunit Volcano, Chaîne des Puys, Massif Central, France. Contributions to Mineralogy and Petrology 149 (5), 600–612.

Kelley, K.A., Cottrell, E., 2009. Water and the oxidation state of subduction zone magmas. Science 325, 605–607.

Khanna, T.C., Sai, V.S., Bizimis, M., Krishna, A.K., 2016. Petrogenesis of ultramafics in the Neoarchean Veligallu greenstone terrane, eastern Dharwar craton, India: constraints from bulk-rock geochemistry and Lu-Hf isotopes. Precambrian Research 285, 186–201.

Kouchi, A., Sugawara, Y., Kashima, K., Sunagawa, I., 1983. Laboratory growth of sector zoned clinopyroxenes in the system $CaMgSi_2O_6$-$CaTiAl_2O_6$. Contributions to Mineralogy and Petrology 83 (1–2), 177–184.

Koutsovitis, P., Magganas, A., 2016. Boninitic and tholeiitic basaltic lavas and dikes from dispersed Jurassic East Othris ophiolitic units, Greece: petrogenesis and geodynamic implications. International Geology Review 58 (16), 1983–2006.

Koutsovitis, P., Magganas, A., Ntaflos, T., 2012. Rift and intra-oceanic subduction signatures in the Western Tethys during the Triassic: the case of ultramafic lavas as part of an unusual ultramafic–mafic–felsic suite in Othris, Greece. Lithos 144, 177–193.

Kunzmann, T., 1999. The aenigmatite – rhönite mineral group. European Journal of Mineralogy 11, 743–756.

Kushiro, I., 1969. The system forsterite-diopside-silica with and without water at high pressures. American Journal of Science 267, 269–294.

Le Bas, M.J., 2000. IUGS reclassification of the high-Mg and picritic volcanic rocks. Journal of Petrology 41 (10), 1467–1470.

MacLeod, C.J., Lissenberg, C.J., Bibby, L.E., 2013. "Moist MORB" axial magmatism in the Oman ophiolite: the evidence against a mid-ocean ridge origin. Geology 41 (4), 459–462.

Maier, W.D., Barnes, S.-J., 2004. Pt/Pd and Pd/Ir ratios in mantle-derived magmas: a possible role for mantle metasomatism. South African Journal of Geology 107 (3), 333–340.

Maurel, C., Maurel, P., 1982. Étude expérimentale de la distribution de l'aluminium entre bain silicaté basique et spinelle chromifère. Implications pétrogénétiques: teneur enchrome des spinelles. Bulletin de Mineralogie 105, 197–202.

Melcher, F., Grum, W., Simon, G., Thalhammer, T.V., Stumpfl, E.F., 1997. Petrogenesis of the ophiolitic giant chromite deposits of Kempirsai, Kazakhstan: a study of solid and fluid inclusions in chromite. Journal of Petrology 38 (10), 1419–1458.

Mole, D.R., Fiorentini, M.L., Thebaud, N., Cassidy, K.F., McCuaig, T.C., Kirkland, C.L., Romano, S.S., Doublier, M.P., Belousova, E.A., Barnes, S.J., Miller, J., 2014. Archean komatiite volcanism controlled by the evolution of early continents. Proceedings of the National Academy of Sciences 111 (28), 10083–10088.

Monjoie, P., Lapierre, H., Tashko, A., Mascle, G.H., Dechamp, A., Muceku, B., Brunet, P., 2008. Nature and origin of the Triassic volcanism in Albania and Othrys: a key to understanding the NeoTethys opening? Bulletin de la Société Géologique de France 179, 411–425.

Pagé, P., Barnes, S.-J., 2009. Using trace elements in chromites to constrain the origin of podiform chromitites in the Thetford Mines Ophiolite, Quebec, Canada. Economic Geology 104, 997–1018.

Paraskevopoulos, G., 1987. Contribution to the study of the ophiolites. Academy Athens 52, 1–207.

Paraskevopoulos, G., Economou, M., 1986. Komatiite-type ultramafic lavas from the Agrilia Formation, Othrys ophiolite complex, Greece. Ofioliti 11 (3), 293–304.

Paraskevopoulos, G., Economou-Eliopoulos, M., 1997. Geochemistry and geotectonic setting of basaltic rocks from the Othrys ophiolite complex. Annales Géologiques des Pays Helléniques 37, 611–612.

Parlak, O., Höck, V., Delaloye, M., 2002. The supra-subduction zone Pozanti–Karsanti ophiolite, southern Turkey: evidence for high-pressure crystal fractionation of ultramafic cumulates. Lithos 65 (1), 205–224.

Pe-Piper, G., 1998. The nature of Triassic extension-related magmatism in Greece; evidence from Nd and Pb isotope geochemistry. Geological Magazine 135, 331–348.

Powell, M.A., Walker, D., Hays, J.F., 1980. Controlled cooling and crystallization of a eucrite-microprobe studies. Lunar and Planetary Science Conference Proceedings 11, 1153–1168.

Puchtel, I.S., Haase, K.M., Hofmann, A.W., Chauvel, C., Kulikov, V.S., Garbe-Schönberg, C.D., Nemchin, A.A., 1997. Petrology and geochemistry of crustally contaminated komatiitic basalts from the Vetreny Belt, southeastern Baltic Shield: evidence for an early Proterozoic mantle plume beneath rifted Archean continental lithosphere. Geochimica et Cosmochimica Acta 61 (6), 1205–1222.

Puchtel, I.S., Blichert-Toft, J., Touboul, M., Walker, R.J., Byerly, G., Nisbet, E.G., Anhaeusser, C.R., 2013. Insights into early Earth from Barberton komatiites: evidence from lithophile isotope and trace element systematics. Geochimica et Cosmochimica Acta 108, 63–90.

Rassios, A., Konstantopoulou, G., 1993. Emplacement tectonism and the position of chrome ores in the Mega Isoma peridotites, SW Othris, Greece. Bulletin of the Geological Society of Greece XXVII/2, 463–474.

Rassios, A., Moores, E., 2006. Heterogeneous mantle complex, crustal processes, and obduction kinematics in a unified Pindos-Vourinos ophiolite slab (northern Greece). In: Robertson, A.H.F., Mountrakis, D. (Eds.), Tectonic Development of the Eastern Mediterranean Region. Geological Society, London, Special Publications 260, pp. 237–266.

Robertson, A.H., Mountrakis, D., 2006. Tectonic development of the Eastern Mediterranean region: an introduction. Geological Society, London, Special Publications 260 (1), 493–505.

Saccani, E., Beccaluva, L., Photiades, A., Zeda, O., 2011. Petrogenesis and tectono-magmatic significance of basalts and mantle peridotites from the Albanian–Greek ophiolites and sub-ophiolitic mélanges. New constraints for the Triassic–Jurassic evolution of the Neo-Tethys in the Dinaride sector. Lithos 124 (3), 227–242.

Sharygin, V.V., Kóthay, K., Szabó, C.S., Timina, T.Ju, Török, K., Vapnik, Ye, Kuzmin, D.V., 2011. Rhönite in alkali basalts: silicate melt inclusions in olivine phenocrysts. Russian Geology and Geophysics (Geologiya i Geofizika) 52 (11), 1334–1352 (1695–1717).

Shaw, C.S., 2009. Textural development of amphibole during breakdown reactions in a synthetic peridotite. Lithos 110 (1), 215–228.

Shea, T., Hammer, J.E., 2013. Kinetics of cooling-and decompression-induced crystallization in hydrous mafic-intermediate magmas. Journal of Volcanology and Geothermal Research 260, 127–145.

Shea, T., Lynn, K.J., Garcia, M.O., 2015. Cracking the olivine zoning code: distinguishing between crystal growth and diffusion. Geology 43 (10), 935–938.

Smith, P.M., Asimow, P.D., 2005. Adiabat_1ph: a new public front-end to the MELTS, pMELTS, and pHMELTS models. Geochemistry, Geophysics, Geosystems 6, Q02004. http://dx.doi.org/10.1029/2004GC000816.

Smith, A.G., Hynes, A.J., Menzies, M., Nisbet, E.G., Price, I., Welland, M.J.P., Ferrière, J., 1975. The stratigraphy of the Othris Mountains, eastern central Greece. Eclogae Geologicae Helvetiae 68, 463–481.

Sossi, P.A., O'Neill, H.S.C., 2016. Liquidus temperatures of komatiites and the effect of cooling rate on element partitioning between olivine and komatiitic melt. Contributions to Mineralogy and Petrology 171:49. http://dx.doi.org/10.1007/s00410-016-1260-x.

Takahashi, E., 1986. Origin of basaltic magmas: implications from peridotite melting experiments and an olivine fractionation model. Journal of the Volcanological Society of Japan 20, S17–S40.

Toplis, M.J., 2005. The thermodynamics of iron and magnesium partitioning between olivine and liquid: criteria for assessing and predicting equilibrium in natural and experimental systems. Contributions to Mineralogy and Petrology 149, 22–39.

Treiman, A.H., 2008. Rhönite in Luna 24 pyroxenes: first find from the Moon, and implications for volatiles in planetary magmas. American Mineralogist 93 (2–3), 488–491.

Tsikouras, B., Karipi, S., Rigopoulos, I., Perraki, M., Pomonis, P., Hatzipanagiotou, K., 2008. Geochemical processes and petrogenetic evolution of rodingite dykes in the ophiolite complex of Othrys (Central Greece). Lithos 113, 540–554.

Walker, D., Kirkpatrick, R.J., Longhi, J., Hays, J.F., 1976. Crystallization history of lunar picritic basalt sample 12002: phase-equilibria and cooling-rate studies. Geological Society of America Bulletin 87 (5), 646–656.

Warren, P.H., Huber, H., Ulff-Möller, F., 2006. Alkali-feldspathic material entrained in Fe, S-rich veins in a monomict ureilite. Meteoritics & Planetary Science 41 (5), 797–813.

Welsch, B., Hammer, J., Baronnet, A., Jacob, S., Hellebrand, E., Sinton, J., 2016. Clinopyroxene in postshield Haleakala ankaramite: 2. Texture, compositional zoning and supersaturation in the magma. Contributions to Mineralogy and Petrology 171 (1), 1–19.

Xiong, F., Yang, J., Robinson, P.T., Gao, J., Chen, Y., Lai, S., 2017. Petrology and geochemistry of peridotites and podiform chromitite in the Xigaze ophiolite, Tibet: implications for a suprasubduction zone origin. Journal of Asian Earth Sciences 146, 56–75.